

Solvable Quantum Circuits in Tree+1 Dimensions

Oliver Breach,^{1,*} Benedikt Placke,¹ Pieter W. Claeys,² and S.A. Parameswaran¹

¹*Rudolf Peierls Centre for Theoretical Physics, Parks Road, Oxford, OX1 3PU, UK*

²*Max Planck Institute for the Physics of Complex Systems, Nöthnitzer Str. 38, Dresden 01187, Germany*

(Dated: March 28, 2025)

We devise tractable models of unitary quantum many-body dynamics on tree graphs, as a first step towards a deeper understanding of dynamics in non-Euclidean spaces. To this end, we first demonstrate how to construct strictly local quantum circuits that preserve the symmetries of trees, such that their dynamical light cones grow isotropically. We show that, for trees with coordination number z , such circuits can be built from z -site gates. We then introduce a family of gates for which the dynamics is exactly solvable; these satisfy a set of constraints that we term ‘tree-unitarity’. Notably, tree-unitarity reduces to the previously-established notion of dual-unitarity for $z = 2$, when the tree reduces to a line. Among the unexpected features of tree-unitarity is a trade-off between ‘maximum velocity’ dynamics of out-of-time-order correlators and the existence of non-vanishing correlation functions in multiple directions, a tension absent in one-dimensional dual-unitary models and their Euclidean generalizations. We give various examples of tree-unitary gates, discuss dynamical correlations, out-of-time-order correlators, and entanglement growth, and show that the kicked Ising model on a tree is a physically-motivated example of maximum-velocity tree-unitary dynamics.

I. INTRODUCTION

The emergence and ongoing development of experimental platforms with precise control over quantum degrees of freedom has paved the way for detailed investigation into out-of-equilibrium quantum systems. These platforms include both analog devices such as ultracold atom simulators [1], Rydberg arrays [2], and trapped ion devices [3], as well as digital platforms such as superconducting qubit arrays [4, 5] where discrete operations may be performed on sets of qubits. Such digital platforms raise new fundamental questions about the nature of many-body quantum dynamics under discrete local gates [6], both regarding novel universal phenomena that may appear, and their utility in describing more general out-of-equilibrium dynamics. Discrete time evolution in the form of ‘brickwork quantum circuits’ has gained intense attention as a minimally structured model for unitary dynamics generated by local interactions [7–10]. These brickwork models can be used to gain theoretical insight into universal aspects of many-body dynamics, and are tailor-made for quantum simulation, being natively realized in digital quantum computing setups.

Analytically studying the properties of such models is challenging. Currently, two main approaches have allowed theoretical progress to be made by simplifying this problem. In the first, randomness is introduced and the focus is shifted to ensemble-averaged dynamics rather than any specific realization; such averaging often allows for an effective description in terms of classical degrees of freedom [7–9]. This approach has proven to be highly successful in understanding the dynamics of operator scrambling and entanglement spreading as well

as phase transitions in these phenomena induced by repeated measurements (for a recent review, see Ref. 10). A second approach is to identify classes of models with special properties that enable analytic treatment. Dual-unitary circuits are a prime example [11, 12], where the discreteness of both space and time can be used to realize dynamics that possesses unitarity in both the space and time directions. Dual-unitary brickwork dynamics is both provably quantum chaotic and exactly solvable, and through the study of these models many of the insights from random circuits could be demonstrated to extend to more structured settings. For instance, dual-unitarity has enabled exact calculation of the dynamics of correlation functions [12, 13], entanglement [11, 14, 15], out-of-time-order correlators [16, 17], deep thermalization [18–21], and Hilbert space delocalization [22]. Dual-unitary circuits have also been realized experimentally in various quantum computing platforms [23–25]. Since the discovery of dual-unitarity, further examples of solvable dynamics have been found, such as triunitarity and round-a-face circuits involving 3-site operators [26–28], in circuits with (2+1)d square lattices [29, 30], and in (1+1)d nonsquare lattices with different space-time symmetries, leading to hierarchical extensions of dual-unitarity [31–35].

While most work in these directions has focused on standard Euclidean geometries, the versatility of quantum devices has now reached a level where this is not a necessary restriction [36–40]. In fact, implementing non-Euclidean geometries may be highly beneficial. For example, they potentially allow the implementation of quantum error correcting codes with far lower overhead [41–45] and, from a more physical perspective [46, 47], have been shown to host unique dynamical and thermodynamic phases of matter [48–53]. Quantum states defined on hyperbolic geometries and constructed out of perfect tensors (a generalization of dual-unitary gates) have also been proposed as minimal mod-

* oliver.breach@physics.ox.ac.uk

els for holography [54–57]. Among non-Euclidean lattice geometries, one of the simplest is that of the Cayley tree. The absence of loops has made trees a fruitful source of analytically solvable statistical mechanics models [58, 59], which can be strikingly different from their Euclidean counterparts [60].

Non-Euclidean lattice geometries explicitly break the symmetry between space and time, such that it is not clear if and how they support a notion of space-time duality. Additionally, the exact solvability of dual-unitary circuits is underpinned by the notion of an operator propagating in a unique ‘maximum velocity’ direction [16], where the more complicated geometry of non-Euclidean lattices typically gives rise to an exponentially growing number of such directions. The corresponding difficulty of simulating the quantum dynamics due to this rapid growth further motivates the study of exactly solvable models of many-body dynamics on tree geometries, the focus of the present work. Before proceeding to a summary of our results, a word of clarification is in order: many existing results on dynamics on trees [59, 61–64] invoke a tree-like tensor network structure of *spacetime*. In contrast, here we exclusively consider the setting where only the spacelike direction is a tree: in other words, the tensor network for the time evolution over discrete time t consists of t tree-like time slices, with local unitary gates acting between time slices [see, e.g. Fig. 1(b) or Fig. 2(b)]. This more closely resembles the kind of evolution we might imagine implementing on a quantum simulator with flexible spatial connectivity, and which would apply in the physical setting of expander-graph constructions of quantum codes. An intuitive and vivid description for our construction, reflected in our title, is that we work in “tree+1” dimensions, with the extra, non-tree-like dimension being time.¹

Since brickwork structures have provided rich insights into local unitary dynamics in the Euclidean context, we begin by extending the concept to the Cayley tree. A naïve generalization of the notion of brickwork circuits in terms of 2-site unitary gates gives rise to highly anisotropic dynamics (Sec. II). Instead, we show that for a tree lattice structure with coordination number z , a brickwork structure in terms of z -site gates should be deployed in order to recover isotropic dynamics (Sec. III A). For the corresponding z -site gates, the notion of dual-unitarity can then be extended to a notion that we dub ‘tree-unitarity’, where the tree geometry results in different space-time isometries (Sec. III B). Dual-unitarity can be realized through kicked Ising dynamics on a one-dimensional lattice, and kicked Ising dynamics on the tree geometry realizes tree-unitarity (Sec. III C). More generally, for $z = 2$, tree-unitary circuits reduce to the familiar dual-unitary brickwork circuits. In both dual-unitary and tree-unitary models, the dynamical correlation functions are restricted to the edge of a causal

light cone (light tree), where they can be exactly calculated using a quantum channel approach (Sec. IV A). Out-of-time-order correlation functions (OTOCs) can be similarly characterized, although tree-unitary circuits no longer automatically exhibit the ballistic spreading with maximal butterfly velocity that is characteristic of dual-unitary circuits (Sec. IV B). Tree-unitarity does result in maximal entanglement growth, where for specific initial states and subregions, the subregion entanglement grows exponentially before saturating at the maximally mixed value (Sec. IV C). A maximal butterfly velocity is recovered upon imposing additional constraints on top of tree-unitarity, which also imply that dynamical correlations along any non-maximal-velocity direction vanish identically (Sec. V). In this way, these models we introduce highlight the features of operator spreading that are particular to the tree geometry, including the proliferation of different paths, the exponential growth of subsystem entanglement, and the trade-off between maximal butterfly velocity and non-vanishing correlation functions. We conclude with a discussion and outlook (Sec. VI).

II. MOTIVATING THE z -SITE UNITARY CIRCUIT CONSTRUCTION

In this section we will sketch an (ultimately unsatisfactory) attempt to construct unitary circuits on the Cayley tree by using 2-site unitary gates in a ‘brickwork’ construction. This initially may seem the most natural way to lift the ideas of dual-unitarity to the tree setting. However, as we show below, any unitary circuit built from two-site gates on a tree will necessarily involve several pathologies. Ultimately, these are linked to the necessity of choosing a sequence in which to apply the z possible 2-site gates at each node, which breaks an extensive number of tree symmetries. The origins of the issue are already visible in the (1+1)d brickwork setting, where the 2-site decomposition necessarily breaks the symmetry between even and odd sites on the lattice. This is exponentially magnified in the tree setting, since there is a sequence choice to be made at *each* node. The end result is a highly anisotropic ‘light cone’ on the tree: the time taken for correlations to spread to different sites at a fixed depth from a given site depends strongly on the specific sequence of steps taken to reach that site, and the resulting order of application of unitaries, violating the (large) set of symmetries of the tree.

To see this more concretely, consider such a 2-site unitary construction applied to the $z = 3$ Cayley tree in Fig. 1(a). We color the bonds of the tree such that no bonds of the same color share a vertex, which prescribes a particular sequence of application of 2-site gates. One such coloring is shown in Fig. 1(a), in which we apply 2-site gates to the orange, blue, and green bonds in sequence, as shown in Fig. 1(b).

Under such a brickwork unitary evolution, an operator initially localized to a single site spreads as shown in

¹ We thank Vedika Khemani for suggesting this terminology.

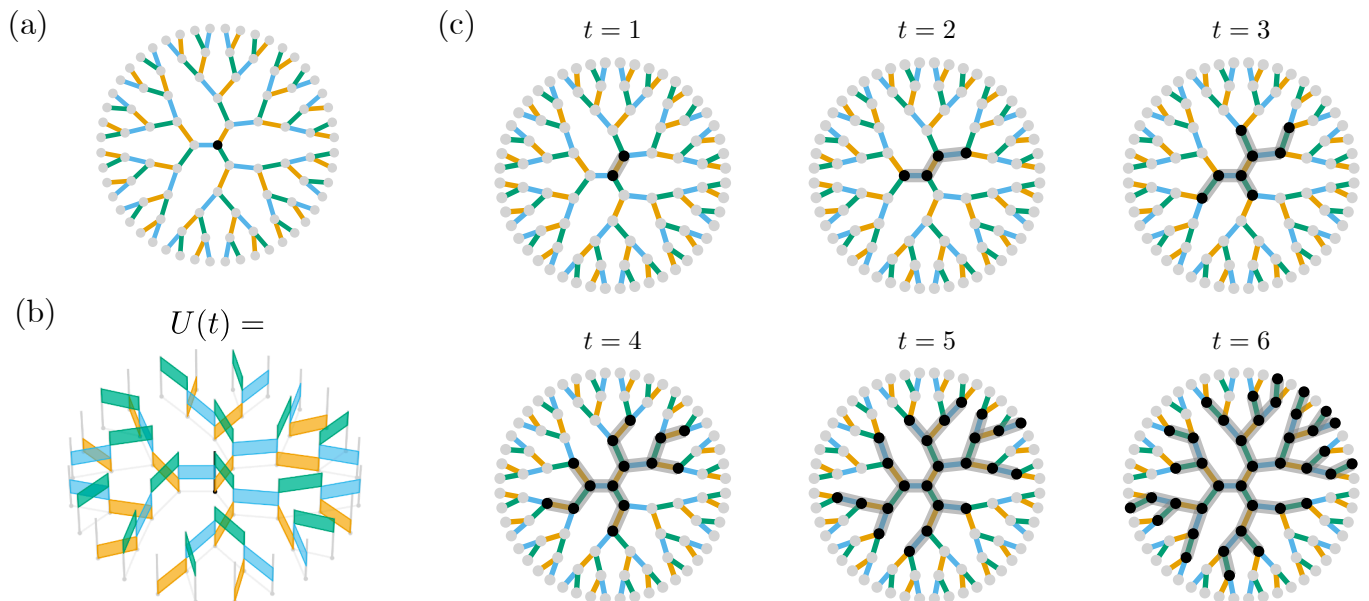


FIG. 1. (a) A coloring of the $z = 3$ tree with 3 colors. A given circuit realization may apply unitaries in the ordering orange, blue, green, for example. (b) The corresponding time-evolution operator for 6 layers (2 full periods). The colored rectangles correspond to the two-site unitary gates, which need not all be identical. (c) The light cone for a circuit constructed by z layers of two-site unitary gates is strongly asymmetric. Here we highlight how an operator initially at the root will spread upon application of layers in the order orange, blue, green. Along a given path, the motion appears as a sequence of steps which may be either ‘fast’ (occur immediately) or ‘slow’ (occur after an additional time step).

Fig. 1(c). To simplify the picture, we only draw the tree and the gates, and highlight by dark shading the possible support of the operator as it evolves. Since $z = 3$, for any step except for the first, there are two ‘forward’ directions in which the operator could spread (for the first step, there are three choices). Since different forward directions by construction have different colors, the forward propagation under the unitary evolution occurs first in one direction, then the other.

Since such choice occurs at *each* vertex, any path between two vertices is characterized by a sequence of ‘fast’ or ‘slow’ steps. In a fast step the support grows immediately along the path, while in a slow step the front waits for one time step before progressing. Consequently, a brickwork construction necessarily produces a highly asymmetric “light cone” (i.e. the boundary of operator support at any time that is consistent with unitarity of all gates), and in particular the existence of a unique “fastest” path. The fastest path is defined by the sequence of sites in the operator support that are farthest from the origin at any given time t .

For brickwork circuits in one dimension, the light cone spreads with the same speed in both directions, with a small anisotropy based on the fact that in the very first step an operator either propagates to the left or right depending on whether it is associated with an even or an odd site. For higher but still finite dimensions, the situation is slightly more involved, but the light cone nevertheless typically retains the discrete symmetry of the lattice, or a subset thereof. For example, 2-site brickwork uni-

tary evolution on the square lattice entails distinguishing ‘fast’ paths between the original site and the corners of the ‘light pyramid’ and slower paths to its perimeter, but preserves the four-fold rotational and two-fold mirror symmetries of the lattice. This should be contrasted with the tree setting: if we consider the ‘root’ of the tree to be at the position of the operator at $t = 0$, then demanding isotropy under the tree symmetries imposes the much more stringent constraint of a uniform operator front at a given depth (possibly up to small differences based on the starting site). Evidently, this is violated by the 2-site brickwork evolution, where the anisotropy occurs *on the light cone*.

While a fundamental property of *any* unitary brickwork construction involving 2-site gates, the consequences of this anisotropy are particularly severe for dual-unitary gates, where (in finite dimension) all the non-trivial correlations lie *on* the light cone. This naïve generalization of dual-unitarity to the tree setting exhibits various somewhat pathological features. The resulting dynamics may be summarized as follows (details are provided in App. D for the interested reader):

- (i) two-point correlation functions vanish everywhere except on the light cone in the direction of the unique fastest path;
- (ii) in the fastest direction, operators spread at the maximum velocity allowed by unitarity;
- (iii) in other directions, operators do not spread at the

maximum velocity allowed by unitarity; and

- (iv) entanglement dynamics can be calculated exactly for special initial states; in such states, the entanglement entropy of any subregion A saturates exponentially quickly in time to its maximal value with $S_A(t) = |A|(1 - (z - 1)^{-t})$ after t time steps, where $|A|$ corresponds to the number of vertices inside A .

While possibly interesting in their own right, these results highlight that the naive extension of dual-unitarity is not particularly appealing, especially from the symmetry perspective. Therefore, it is clearly desirable to identify a different generalization of the brickwork construction and of dual-unitarity that preserves more of the symmetries of the tree. In the remainder of this paper, we address this question by introducing the distinct notion of ‘tree-unitarity’, and exploring its consequences.

III. z -SITE UNITARY CIRCUITS AND ‘TREE-UNITARITY’

From the results of the previous section, it is clear that the coordination number of the tree should be directly reflected in the choice of unitary gates. In this section, we introduce a different approach to unitary dynamics on trees based on groupings of z -site operators, which presents a more natural generalization of circuit dynamics (both unitary and dual-unitary) to the tree setting. In other words, the ‘natural’ Trotterization of unitary dynamics on trees involves 2-colorings of the tree into z -site gates, rather than z -colorings into 2-site gates. Extensions of dual-unitarity can be formulated for these circuits in a direct way, and we will identify the necessary set of conditions leading to the analogous property, which we dub ‘tree-unitarity’. Imposing these conditions results in solvable dynamics of correlation functions, out-of-time-order correlation functions, and entanglement, while avoiding the pathological behavior highlighted in the preceding section.

A. Isotropic unitary dynamics on trees

As a first step, recall that the conventional brickwork Trotter decomposition in one dimension separates the unitary evolution into gates acting on even and odd bonds. In the same spirit, for dynamics on a tree we can identify two ‘layers’ of the time evolution by decomposing the bonds of the tree into two sets².

² Such a decomposition is also used for algorithms such as infinite time-evolving block decimation on a tree [65], where taking z -site gates allows as much symmetry as possible to be preserved when Trotterizing the evolution.

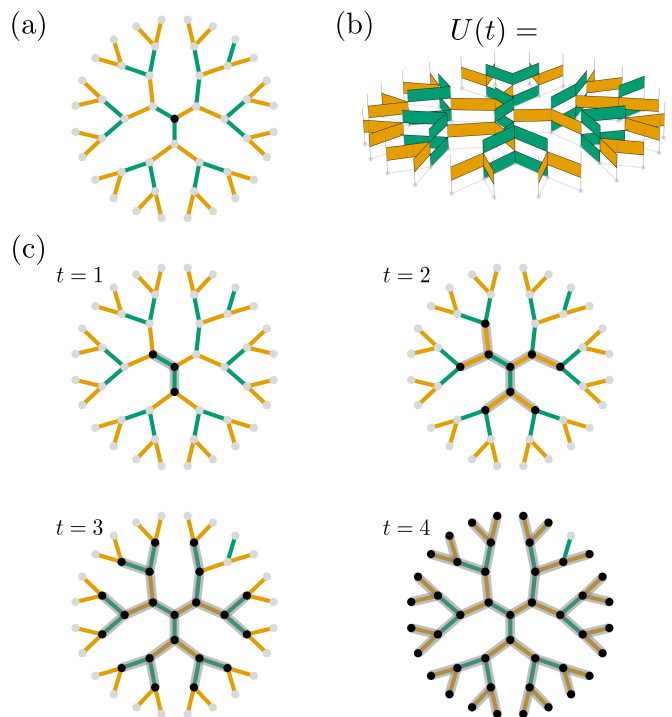


FIG. 2. (a) A coloring of the $z = 3$ Cayley tree into two sets of 3-site unitaries. (b) The corresponding time-evolution operator for 3 layers (1.5 full periods). (c) The light cone for a circuit constructed by 2 layers of z -site gates generates a symmetric light cone, here highlighted in grey.

To do so, we iteratively ‘grow’ a 2-coloring of the edges of the tree into green and orange sets (Fig. 2(a)) by alternating between odd and even steps as follows. In an odd step, we consider each vertex on the boundary of the 2-colored region, and ensure that exactly one of its z neighbours is green and the remaining $z - 1$ are orange. In an even step, we do the converse, i.e. ensure that exactly one of the neighbours is orange and the remaining $z - 1$ are green. Iterating this procedure generates a 2-coloring of the tree edges that partitions it into clusters of z vertices connected by edges of the same color, such that every vertex (in the finite case, every vertex that is not a leaf of the tree) belongs to exactly two clusters of opposite color. We can then apply z -site unitary gates to all the clusters of a given color in one time step, and then apply them to clusters of the opposite color in the next time step, thereby directly generalizing the two-layer unitary circuits from one dimension to the tree setting.

We now show that this decomposition into z -site unitaries leads to an isotropic light cone, with the same velocity in any direction, up to a possible correction of a single time step (similar to the odd-even anisotropy in one dimension). Specifically, we prove that the number of time steps $t_{i \rightarrow j}$ for an operator initially localized at site i to spread to site j satisfies the inequality

$$r_{i,j} - 1 \leq t_{i \rightarrow j} \leq r_{i,j} + 1, \quad (1)$$

where $r_{i,j}$ is the graph distance between i and j .

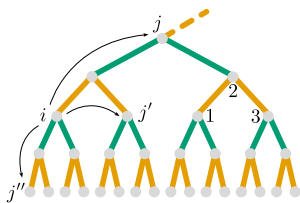


FIG. 3. For a pair of nodes i, j separated by a fixed graph distance, the path joining them can turn away from the root at most once. The time taken for an operator to spread from i to any possible j at fixed distance can therefore differ by at most 2 time steps. To the right side of the tree, we also show the labeling convention for the legs of a $z = 3$ gate on the tree.

To see this, first observe that there is a unique path that connects i and j on the tree; the 2-coloring of the graph edges then induces an edge coloring of this path. Given our layered unitary construction, at any time step the operator front can advance from its current site to any site linked to it by (one or more) edges of the same color. Thus, depending on whether the first gate applied is the same or opposite color as the first edge of the path, we see that $t_{i,j} = n_c$ or $t_{i,j} = n_c + 1$, where n_c is the number of edge color changes in the path, and the offset in the second case captures the need to wait for a single time step at the outset before the front starts moving. To determine n_c , we can take the two sites to be part of some rooted tree; this can always be done without loss of generality assuming a sufficiently large system. The 2-coloring then guarantees that each z -site cluster has one site at depth d and $z - 1$ sites at depth $d + 1$ relative to this root. Now, any path between two sites i and j at a fixed distance $r_{i,j} = r$ from each other involves r_+ steps ‘upwards’ towards the root and r_- steps ‘downwards’ towards the leaves, with $r_+ + r_- = r$. Evidently, paths with $r_+ = 0$ or $r_- = 0$ never ‘turn away’ from the root, and it is straightforward to see that the edges along such paths strictly alternate between colors, so that $n_c = r$. The only other possibility is that the path turns exactly once; in this case, the two edges adjacent to the turning vertex are of the same color, and the rest strictly alternate as before, so that $n_c = r - 1$. Combining the results for n_c with those for $t_{i \rightarrow j}$, we arrive at the inequality in (1).

B. Tree-unitarity

For brickwork circuits, imposing additional unitarity constraints such as dual-unitarity has given rise to a wealth of solvable models. Here, we extend these notions to dynamics on trees. Focusing again on $z = 3$ for concreteness, where extensions to arbitrary z are direct, we consider unitary three-site gates which we graphically

represent as

$$U = \text{blue box}, \quad U^\dagger = \text{red box}. \quad (2)$$

Introducing a ‘folded’ notation (the graphical equivalent of the operator-to-state mapping), we can write the superoperator that implements unitary conjugation by U and U^\dagger as

$$\text{folded U} = \text{folded U}^\dagger. \quad (3)$$

Unitarity can then be graphically represented via

$$UU^\dagger = \text{folded U} \text{ folded U}^\dagger = \text{purple box} = \text{circles} = \text{vertical lines} \quad (4)$$

and

$$U^\dagger U = \text{purple box} = \text{circles} = \text{vertical lines}. \quad (5)$$

This folded notation will prove to be convenient when describing operator dynamics.

In order to extend dual-unitarity to the Cayley tree and obtain solvable dynamics, we consider gates that satisfy the additional properties

$$\text{folded U} = \text{folded U}^\dagger = \text{folded U}^\dagger = q^{z-2} \text{circles}, \quad (6)$$

with q the dimension of the local Hilbert space and $z = 3$ in this example. These constraints can be extended to more general z , in which we trace over $z - 1$ pairs of sites and require that we obtain a term proportional to the identity. We denote this set of conditions *tree-unitarity*.

Expressed in the components of U , these conditions read

$$\begin{aligned} \sum_{ijlm} U_{lmn}^{ijk} (U^\dagger)_{ijf}^{lmc} &= \sum_{ijlm} U_{mnl}^{jki} (U^\dagger)_{jfi}^{mcl} \\ &= \sum_{ijlm} U_{nlm}^{kij} (U^\dagger)_{fij}^{clm} = \delta_f^k \delta_n^c. \end{aligned} \quad (7)$$

As will be shown in the next section, tree-unitarity results in dynamics that exhibits the same qualitative behavior as for dual-unitarity, in that, strikingly, all dynamical correlation functions vanish everywhere except on the edge of the causal light cone.

The conditions are qualitatively similar to dual-unitarity, but the tree structure results in some crucial differences. The conditions from Eq. (6) impose that the unitary gates are isometries from the composite Hilbert

spaces corresponding to any pair of opposite legs to the remaining $2(z-1)$ legs.³ This is to be contrasted with the dual-unitarity condition for 2-site gates where the single additional condition is that of *unitarity*; for z -site gates with $z > 2$, the z additional conditions are necessarily modified to isometries. Dual-unitarity is explicitly recovered for $z = 2$ (note that the two possible ways of writing (6) for $z = 2$ lead to equivalent conditions, which is not the case for $z > 2$). For $z = 3$, the tri-unitary gates introduced in Ref. 26 can be deformed into 3-site tree-unitary gates (see App. B3). However, gates constructed this way are non-generic (in a sense made precise in Sec. V), with tree-unitarity gates presenting a much broader class, and are furthermore not restricted to $z = 3$.

C. Kicked Ising Model

It is natural to ask if and how tree-unitary gates can be constructed for different coordination number z and local Hilbert space dimensions q . Numerically, tree-unitary gates can be constructed in a straightforward manner through an extension of the algorithm proposed in Ref. 66 for the construction of dual-unitary gates, as detailed in App. A. A numerical estimation of the dimension of the manifold of tree-unitary gates using the approach of Ref. 27 suggests that, for 3-site gates with $q = 2$, tree-unitary gates form a 37-dimensional space. This dimension is substantially smaller than that of the space of 3-site unitary operators on qubits, which has dimension 64, but nevertheless is a large parameter space containing a range of interesting behaviour.

A particular tree-unitary circuit can be obtained by considering kicked Ising dynamics. The self-dual kicked Ising model is a paradigmatic realization of dual-unitary dynamics [11, 18, 21, 67–69] and can be directly extended to the Cayley tree. While the resulting gates do not exhaust the full space of tree-unitary gates, and are in some aspects nongeneric, this model serves to both highlight that tree-unitary gates can be constructed for any coordination number z , and introduces a circuit that is naturally realized in (Hamiltonian) Floquet dynamics.

We motivate this construction by first considering Floquet dynamics on a Cayley tree, with every vertex supporting a spin-1/2 degree of freedom. Dynamics under a classical Ising Hamiltonian H_I is periodically alternated

with a transverse kick H_K , where

$$H_I = J \sum_{\langle i,j \rangle} \sigma_i^z \sigma_j^z + \sum_i h_j \sigma_j^z, \quad H_K = b \sum_j \sigma_j^y. \quad (8)$$

Here the Ising interaction acts on neighboring sites $\langle i, j \rangle$, J and b are the Ising interaction strength and the transverse kick strength, respectively, and σ_i^α with $\alpha \in \{x, y, z\}$ are the Pauli matrices. $\{h_j\}$ describes a (possibly inhomogeneous) longitudinal field. The dynamics after t periods can be written as

$$U(t) = (e^{-iH_K} e^{-iH_I})^t, \quad (9)$$

where we have absorbed all time scales into the couplings in H_I and H_K . When restricted to a one-dimensional lattice, this dynamics can be recast as a dual-unitary circuit at the parameter values $J = b = \pi/4$ [70]. On the Cayley tree, it is now possible to recast this dynamics as a tree-unitary circuit. Introducing 2-site Ising gates and 1-site kicked gates as

$$\mathcal{I}_{12} = e^{-iJ\sigma_1^z\sigma_2^z - i(h_1\sigma_1^z + h_2\sigma_2^z)/2}, \quad \mathcal{K} = e^{-ib\sigma^y}, \quad (10)$$

we can identify the dynamics with a unitary circuit generated by arranging z -site gates according to the geometry shown in Fig. 2. The constituting gates are of the form

$$U = \prod_{\langle i,j \rangle} \mathcal{I}_{ij} \prod_{j=1}^z \mathcal{K}_j \prod_{\langle i,j \rangle} \mathcal{I}_{ij}, \quad (11)$$

where the Ising gates act on all neighboring sites inside the cluster of z sites. These gates satisfy the tree-unitary property [Eq. (6)] for the dual-unitary parameters $|J| = |b| = \pi/4$. Note that U reduces to a Clifford gate if $h_j = \mathbb{Z}\pi/8, \forall j$; this fact allows for numerical simulations of tree-unitary dynamics for large system sizes.

It is easiest to see that that gates of this form satisfy tree-unitarity using the graphical tensor network language of Refs. 18 and 21. By introducing the building blocks

$$\begin{array}{c} | \\ \hline \\ | \end{array} = \frac{1}{\sqrt{2}} \begin{pmatrix} 1 & -i \\ -i & 1 \end{pmatrix} = H, \quad \begin{array}{c} a \\ | \\ \hline \\ c \end{array} = \delta_{abc} e^{-ig(1-2a)}, \quad (12)$$

we can write the Ising and kick terms as

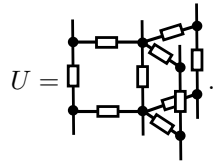
$$\mathcal{I}_{12} = \begin{array}{c} \bullet \quad \bullet \\ | \quad | \\ \hline \\ | \quad | \\ \bullet \quad \bullet \end{array} \frac{\pi}{4}, \quad \mathcal{K} = \begin{array}{c} | \\ \hline \\ | \end{array} \frac{\pi}{2}. \quad (13)$$

In terms of these, the $z = 3$ gate (11) can be graphically represented as

$$U = \begin{array}{c} \bullet \quad \bullet \quad \bullet \\ | \quad | \quad | \\ \hline \\ | \quad | \quad | \\ \bullet \quad \bullet \quad \bullet \end{array}, \quad (14)$$

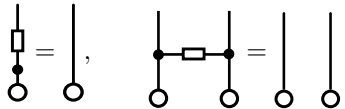
³ Experts may recognize a family resemblance to $2z$ -leg *perfect tensors*, which are isometries from *any* set of $z' \leq z$ legs to the remaining $2z - z'$ legs. This is equivalent, when all the legs are identical, to *unitarity* for any *balanced* bipartition where $z' = z$. The tree-unitary constraints are weaker than this, since they only require isometry for bipartitions with $z' = 2$ and legs on opposite sides. Perfect tensors are thus a subset of tree-unitary gates, with special features discussed in Sec. V.

where we have suppressed writing the phases in the δ -tensors. Similarly, the $z = 4$ gate is



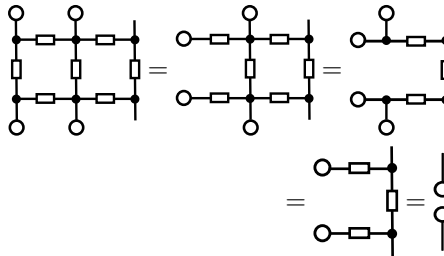
$$U = \text{[Diagram]} \quad (15)$$

In proving identities such as tree-unitarity, it is useful to note that in the folded representation,



$$\text{[Diagram]} = \text{[Diagram]}, \quad \text{[Diagram]} = \text{[Diagram]} \quad (16)$$

Using these, we can show that the KIM satisfies tree-unitarity as follows



$$\text{[Diagram]} = \text{[Diagram]} = \text{[Diagram]} = \text{[Diagram]} \quad (17)$$

This derivation directly extends to the remaining tree-unitary conditions and arbitrary z .

IV. DYNAMICS OF TREE-UNITARY CIRCUITS

Having introduced the basic structure and established the isotropy of the light cone, we now consider the dynamics of circuits on the tree. We focus on two-point correlation functions, out-of-time-order correlation functions, and entanglement growth following a quench. All the results of this section apply to *any* tree-unitary circuit; in the following Sec. V, we discuss special cases which constrain the dynamics further. Note that we will generally consider dynamics on the infinite Bethe lattice (regular tree). However, due to the causal structure of the circuit, dynamics can be restricted to the Cayley tree with the leaves on the edge of the causal light cone without loss of generality.

A. Correlation Functions

We first consider two-point correlation functions of the form

$$c_{\alpha\beta}(i, j; t) = \langle \sigma_\beta(i, 0) \sigma_\alpha(j, t) \rangle, \quad (18)$$

at infinite temperature, with $\langle \bullet \rangle \equiv \text{tr}(\bullet)/\text{tr}(\mathbb{1})$. Here $\sigma_{\alpha,\beta}$ are (possibly generalized) Pauli matrices satisfying $\text{tr}(\sigma_\alpha \sigma_\beta)/q = \delta_{\alpha\beta}$ for local Hilbert space dimension q .

Identifying $\sigma_0 = \mathbb{1}$, all other Pauli matrices are fixed to be traceless and chosen to be Hermitian, and we will focus on $\alpha, \beta \neq 0$ in what follows. We take $\sigma_\alpha(j)$ to act as σ_α on site j and as the identity everywhere else and define the dynamics as $\sigma_\alpha(j, t) = U(t)^\dagger \sigma_\alpha(j) U(t)$.

The correlation function (18) vanishes due to unitarity whenever one Pauli operator lies outside the light cone of the other. While correlation functions inside this light cone are generally exponentially costly to compute, correlation functions *on* the light cone admit an efficient calculation in terms of quantum channels [12, 16]. For dual-unitary circuits, correlation functions inside the causal light cone additionally vanish due to the space-time duality, such that the only nonzero correlations are those on the edge of the causal light cone.

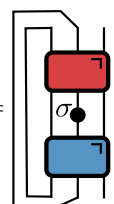
On the tree, we again have vanishing correlation functions outside the light cone, and correlation functions inside the light cone are exponentially costly to compute in general. On the edge of the light cone, we can calculate the correlation functions using quantum channels $\mathcal{M}_{e\tilde{e}}(\sigma)$ with $e, \tilde{e} \in \{1, 2, \dots, z\}$. The action of these channels is defined by conjugating the operator on incoming leg e with U , then tracing over all legs apart from $\tilde{e} \neq e$:

$$\mathcal{M}_{e\tilde{e}}(\sigma) = \overline{\text{tr}}_{\tilde{e}} [U^\dagger \sigma(e) U] / q^{z-1}, \quad (19)$$

where $\overline{\text{tr}}_{\tilde{e}}(\dots)$ denotes a trace over all except

the ‘outgoing’ leg \tilde{e} and $\sigma(e) = \mathbb{1}^{\otimes e-1} \otimes \sigma \otimes \mathbb{1}^{\otimes z-e}$ is fixed by the ‘incoming’ leg e . Observe that the case $e = \tilde{e}$ can never appear on the light cone, since this would correspond to the operator moving inside the light cone. We will also write $\mathcal{M}_{e\tilde{e}}(\sigma) \equiv \mathcal{M}_{e\tilde{e}|\sigma}$, since these quantum channels can be interpreted as [super]operators acting on an [operator] Hilbert space spanned by the σ_α . We define an inner product in this operator Hilbert space as $(\sigma_\alpha | \sigma_\beta) \equiv \text{tr}(\sigma_\alpha^\dagger \sigma_\beta)/q$, which will help to simplify the following expressions.

For fixed z , there are $z(z-1)$ choices of such quantum channels. Graphically, these can be represented as, for example (again fixing $z = 3$ for concreteness),

$$\mathcal{M}_{23}(\sigma) = \frac{1}{q^2} \text{tr}_{12} [U^\dagger (\mathbb{1} \otimes \sigma \otimes \mathbb{1}) U] = \text{[Diagram]} \quad (20)$$


or in the folded representation, with all other $z = 3$ channels,

$$\mathcal{M}_{23}|\sigma\rangle = \text{[diagram]}, \mathcal{M}_{21}|\sigma\rangle = \text{[diagram]}, \mathcal{M}_{12}|\sigma\rangle = \text{[diagram]},$$

$$\mathcal{M}_{13}|\sigma\rangle = \text{[diagram]}, \mathcal{M}_{31}|\sigma\rangle = \text{[diagram]}, \mathcal{M}_{32}|\sigma\rangle = \text{[diagram]}.$$

(21)

Light-cone correlation functions between two operators can be calculated through the successive application of such quantum channels, where the precise sequence depends on the path, as we explain below. The argument is identical in most respects to the quantum channel construction for (1+1)d brickwork circuits (see, e.g., Refs. 12 and 16), so we here only quote the final result and comment on key distinctions. We consider the path for an operator initially localized at site i to spread to site j as outlined in Sec. III A, and fix the number of time steps $t = t_{i \rightarrow j}$. The path connecting i and j consists of a set of vertices (v_1, v_2, \dots, v_t) , with $v_1 = i$ and $v_t = j$. For the gate that spreads the operator from v_τ to $v_{\tau+1}$, we take e_τ to be the leg acting on v_τ and \tilde{e}_τ to be the leg acting on $v_{\tau+1}$. The resulting correlation function reads

$$c_{\alpha\beta}(i, j; t) = (\sigma_\beta | \mathcal{M}_{e_t \tilde{e}_t} \dots \mathcal{M}_{e_2 \tilde{e}_2} \mathcal{M}_{e_1 \tilde{e}_1} | \sigma_\alpha). \quad (22)$$

This expression can be efficiently evaluated for arbitrarily long times. One key difference from the (1+1)d case is already apparent in the freedom to choose a (nearly) arbitrary set of ingoing and outgoing legs of the $\mathcal{M}_{e\tilde{e}}$ in (22). This stems from the fact that there are many distinct paths and hence choices of e, \tilde{e} that remain on the light cone, in contrast to the (1+1)d case where there is a unique choice (so that, for example, propagation along the left light cone is generated by repeated iterations of the channel \mathcal{M}_{12} , and along the right light cone by iterations of \mathcal{M}_{21}). For a tree with the layout as in Fig. 2, one can clearly make several more choices depending on the precise choice of path, with one important constraint: the ‘‘single-turn’’ rule (that we used in our proof of isotropy in Sec. III A) means that there can be at most one appearance of a channel of the form $\mathcal{M}_{e\tilde{e}}$ for which e and \tilde{e} are *both* ‘leaf’ legs. Here, the terms ‘leaf’ and ‘root’ leg refer to the location of the legs of the gate, with respect to the rooted tree on which we are considering the light cone, as in our discussion in Sec. III A; each gate acts on z sites, the ‘root’ of which is nearest-neighbour to all $z - 1$ ‘leaf’ sites. The resulting exponentially growing choice of channels to apply is in accord with the exponentially growing light cone on the tree.

These quantum channels are unital, i.e. they satisfy $\mathcal{M}_{ij}|\mathbb{1}\rangle = |\mathbb{1}\rangle$, similar to the quantum channels appearing in dual-unitarity. As such, the identity is a trivial eigenoperator with eigenvalue one. For ergodic dynamics the

remaining eigenvalues generally lie inside the unit circle, such that the correlation functions decay exponentially with the graph distance. To illustrate this construction, let us consider the correlation function down the right-most path in Fig. 3. For each step, the ingoing leg is $e = 2$ and the outgoing site is $\tilde{e} = 3$, such that the correlation function is

$$c_{\alpha\beta}(i, j; t) = (\sigma_\beta | \mathcal{M}_{23}^t | \sigma_\alpha) = \text{tr} [\sigma_\beta \mathcal{M}_{23}^t(\sigma_\alpha)] / q. \quad (23)$$

On the other hand, a path that departs from this at the very last leaf, for example, is characterized by

$$\begin{aligned} c_{\alpha\beta}(i, j; t) &= (\sigma_\beta | \mathcal{M}_{21} \mathcal{M}_{23}^{t-1} | \sigma_\alpha) \\ &= \text{tr} [\sigma_\beta \mathcal{M}_{21} \mathcal{M}_{23}^{t-1}(\sigma_\alpha)] / q, \end{aligned} \quad (24)$$

and so on.

All we have used at this stage is that the evolution on the tree is generated by unitary z -site gates. In principle, we could develop expressions similar to (22) for two-point correlation functions *anywhere*, but the dimensions of the corresponding superoperators, and hence the complexity of the computations, grow exponentially in the distance off the light cone. In the (1+1)d case, a crucial simplification is that imposing dual-unitarity results in two-point correlation functions that vanish *everywhere inside* the light cone [12]. As a result, we can calculate *all* two-point correlation functions efficiently, leading to the ‘solvability’ of such circuits. This argument directly extends to our z -site construction on imposing tree-unitarity. In order to show this, it is useful to reinterpret the tree-unitarity conditions [Eq. (6)] on the level of operator spreading. For a general z -site unitary gate acting on sites $1, 2, \dots, z$, the unitary transformation of a single-site Pauli matrix generally returns a linear combination of products of Pauli matrices,

$$U^\dagger \sigma_\alpha(i) U = \sum_{\alpha_1, \alpha_2, \dots, \alpha_z} c_{\alpha_1 \alpha_2 \dots \alpha_z}^{(\alpha, i)} \sigma_{\alpha_1} \otimes \sigma_{\alpha_2} \otimes \dots \otimes \sigma_{\alpha_z}. \quad (25)$$

Correlation functions probe the terms in the expansion where only a single Pauli matrix is nontrivial (different from the identity), since due to the trace-orthonormality of the Pauli matrices

$$\text{tr}[\sigma_\beta(j) U^\dagger \sigma_\alpha(i) U] = c_{0 \dots 0 \alpha_j = \beta 0 \dots 0}^{(\alpha, i)}. \quad (26)$$

Tree-unitarity now strongly constrains the terms that can appear in the right-hand side of (25), enforcing that terms with a single nontrivial Pauli matrix can only appear when this Pauli matrix is located on the edge of the causal light cone, similar to how dual-unitarity enforces maximal operator spreading [16].

Again turning to $z = 3$ tree-unitary gates for concreteness, we can use tree-unitarity to constrain e.g. the evolution of a Pauli matrix located on the second site, $\sigma_\alpha(2)$,

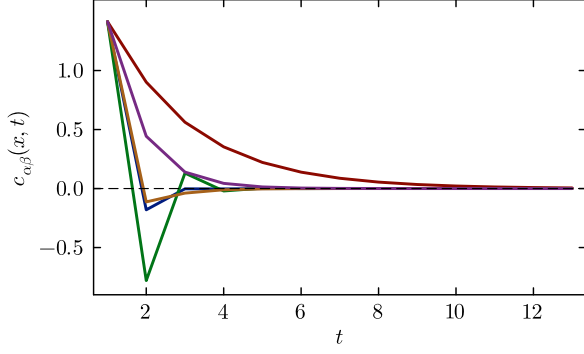


FIG. 5. Correlation function $c_{\alpha\beta}(x, t)$ on the light cone direction $2 \rightarrow 3$ plotted with $\sigma_\alpha = \frac{1}{\sqrt{2}}(X + Z)$ and $\sigma_\beta = Z$, for three random tree-unitary gates generated using the method in App. A.

pinned by the nature of operator spreading in these circuits. We now consider the out-of-time-order correlation function (OTOC) as a different probe of operator spreading, which will be useful in highlighting how moving from dual-unitarity to tree-unitarity induces qualitative changes in the dynamics. The OTOC is defined as

$$C_{\alpha\beta}(i, j; t) = \langle \sigma_\beta(i, 0) \sigma_\alpha(j, t) \sigma_\beta(i, 0) \sigma_\alpha(j, t) \rangle. \quad (28)$$

Outside the light cone, the OTOC always takes the trivial value of 1 because $\sigma_\alpha(0, t)$ and $\sigma_\beta(x, 0)$ commute. In generic unitary circuits, the OTOC develops a front which propagates ballistically at the butterfly velocity $v_B < 1$ and broadens diffusively [7]. For (1+1)d circuits consisting of dual-unitary gates, the butterfly velocity takes its maximally allowed value $v_B = 1$ consistent with the strict light cone, with such circuits referred to as ‘maximum velocity’ [16, 71]. This maximum velocity has been experimentally observed in quantum simulators [24]. In recent years, various circuits exhibiting differing degrees of solvability have been identified, all of which exhibit such a maximum velocity [32, 34], suggesting a strong connection between maximum butterfly velocity and solvability. Remarkably, in tree-unitary circuits this connection breaks down.

We restrict our analysis below to the OTOC on the edge of the causal light cone, and find that tree-unitarity alone does not lead to a nontrivial OTOC on the light cone, indicating a ‘butterfly velocity’ that is not maximal. In (1+1)d circuits, the OTOC value on the light cone can be efficiently calculated using a quantum channel approach [16], and a similar result applies on the tree, where the results of the preceding section can be directly extended to obtain a quantum channel representation of the OTOC on the light cone. This can be expressed in terms of quantum channels involving two copies of the unitary gate and its conjugate (i.e. two replicas). We

define

$$\text{[Diagram]} = \text{[Diagram]} \quad (29)$$

along with the contractions

$$\text{[Diagram]} = \frac{1}{\sqrt{q}} \text{[Diagram]}, \quad \text{[Diagram]} = \frac{1}{\sqrt{q}} \text{[Diagram]}, \quad (30)$$

and superoperators

$$(\sigma| = \text{[Diagram]} = \frac{1}{\sqrt{q}} \text{[Diagram]}, \quad |\sigma\rangle = \text{[Diagram]} = \frac{1}{\sqrt{q}} \text{[Diagram]}. \quad (31)$$

The channel $\mathcal{T}_{e\bar{e}}$ used to compute the OTOC can then be written graphically; for example,

$$\mathcal{T}_{23}|\sigma\rangle = \text{[Diagram]}. \quad (32)$$

Using unitarity and the geometry of the circuit, the light-cone OTOC can be directly expressed as

$$C_{\alpha\beta}(i, j; t) = (\sigma_\beta | \mathcal{T}_{e_t \bar{e}_t} \dots \mathcal{T}_{e_2 \bar{e}_2} \mathcal{T}_{e_1 \bar{e}_1} | \sigma_\alpha). \quad (33)$$

The derivation is analogous to that for (1+1)d unitary circuits [16], so we do not give it here in full and only cite the final result.

The maximal velocity property for dual-unitary circuits corresponds to showing that this OTOC decays to a nontrivial value. To do so, one can study the eigenspectrum of the relevant quantum channel, to characterize the nondecaying eigenoperators. Unitarity alone requires the existence of at least a single left and right eigenoperator with eigenvalue 1,

$$|R\rangle = \text{[Diagram]}, \quad \langle L| = \text{[Diagram]}. \quad (34)$$

In isolation, however, this unitarity condition does not lead to a nontrivial behavior of the OTOC, which is sensible: maximal velocity is not a property of generic unitary circuits. If this is the only eigenoperator with unit-modulus eigenvalue, then the late-time behavior of the OTOC follows as a projection on these eigenoperators and

$$\lim_{t \rightarrow \infty} C_{\alpha\beta}(i, j; t) = (\sigma_\alpha | R) (L | \sigma_\beta) = \text{[Diagram]} = \frac{1}{q^2} \text{tr}[\sigma_\alpha^2] \text{tr}[\sigma_\beta^2] = 1, \quad (35)$$

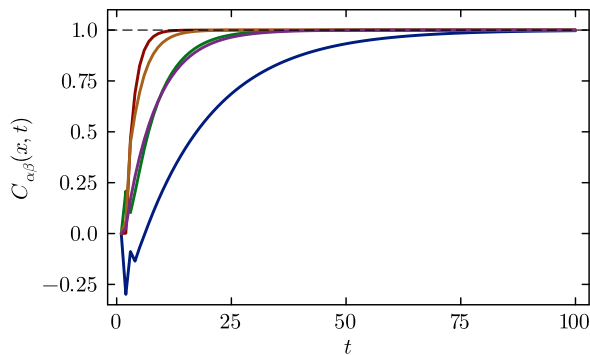


FIG. 6. OTOC $C_{\alpha\beta}(x, t)$ on the light cone direction $2 \rightarrow 3$ with $\sigma_\alpha = \frac{1}{\sqrt{2}}(X + Z)$ and $\sigma_\beta = Z$, for the same random tree-unitary gates as in Fig. 5. The OTOC approaches the trivial value of 1 on the light cone, indicating that operators do not spread at maximum velocity.

where both overlaps vanish because the Pauli matrices are traceless. Without any further structure imposed, there are generically no other unit-eigenvalue eigenoperators, so the OTOC approaches the trivial value of 1, as shown in Fig. 6. This indicates that the butterfly velocity $v_B < 1$.

Imposing dual-unitarity in (1+1)d forces the existence of nontrivial non-decaying eigenoperators. Following the argument above, we then obtain a nontrivial value of the OTOC on the light cone, and hence a maximal velocity $v_B = 1$. We will return to this argument and the explicit construction of such eigenoperators in Sec. V.

In striking contrast to this, while imposing tree-unitarity facilitates solvability (by forcing causal correlators to vanish off the light cone) just as in dual-unitary circuits, it *does not* allow us to construct further unit-eigenvalue eigenoperators to the channels $\mathcal{T}_{e\bar{e}}$ relevant to computing the OTOCs. Numerical inspection of the eigenspectrum of the lightcone channels for a ‘generic’ tree-unitary circuit (from the construction in App. A) shows that indeed no additional such eigenoperators exist. Thus, we conclude that a generic tree-unitary circuit has butterfly velocity $v_B < 1$ along any given path. However, in Sec. V we will see that tree-unitary gates can also obey stronger additional constraints which *do* give $v_B = 1$ in some directions, analogous to the situation in finite dimensions.

The reason for this difference relative to dual-unitary circuits is that while dual-unitarity requires the operator front to grow with every time step, tree-unitarity does not. For dual-unitary 2-site gates $U^\dagger(\sigma \otimes \mathbb{1})U$ consists of a linear combination of $\mathbb{1} \otimes \sigma$ and $\sigma \otimes \sigma$, such that the operator front always moves a single step to the right. However, tree-unitarity implies that e.g. $U^\dagger(\mathbb{1} \otimes \sigma \otimes \mathbb{1})U$ can have contributions of the form $\sigma \otimes \mathbb{1} \otimes \sigma$, $\mathbb{1} \otimes \mathbb{1} \otimes \sigma$ and $\sigma \otimes \mathbb{1} \otimes \mathbb{1}$. While single-site Pauli matrices necessarily ‘hop’ at every time step, this does not imply that the operator front also grows: for instance, the contribution

$\mathbb{1} \otimes \mathbb{1} \otimes \sigma$ does not grow the front along the ‘leftmost’ direction. This freedom to ‘hop’ single-site Paulis without growing the operator front in all directions is again due to the growing number of sites on the light cone on the tree, to be contrasted with the constant number of sites on the light cone in the (1+1)d brickwork circuit.

C. Entanglement Dynamics

Both dual-unitarity and tree-unitarity can be used to obtain exact results for state dynamics in the Schrödinger picture, in addition to the operator dynamics in the Heisenberg picture considered so far. For dual-unitary circuits, such computations rely on the existence of special classes of ‘solvable’ initial states that do not break spatial unitarity, and for which the dynamics of entanglement can be exactly characterized [72]. These states thermalize exactly after a fixed number of time steps, i.e. their reduced density matrix reduces to the maximally mixed state that maximizes the entropy.

The simplest example of a solvable state for a dual-unitary circuit is a product wave function consisting of Bell states on alternating bonds [72]. We now show that (generalized) GHZ states on z sites furnish a natural extension of solvable states to tree-unitary dynamics. The resulting states also exhibit maximal entanglement growth, which is now exponential because of the geometry of the tree, to be contrasted with the linear growth exhibited in (1+1)d brickwork circuits. We consider GHZ states of the form

$$|\text{GHZ}\rangle = \frac{1}{\sqrt{q}} \sum_{a=1}^q |a, a, \dots, a\rangle. \quad (36)$$

These states can be interpreted as isometries in the folded picture. The GHZ states satisfy

$$\overline{\text{tr}}_e(|\text{GHZ}\rangle\langle\text{GHZ}|) = \mathbb{1}_e, \quad (37)$$

for all e , which can be compared with the tree-unitarity conditions [Eq. (6)].

Considering again $z = 3$ for concreteness, the GHZ state can be represented as

$$|\text{GHZ}\rangle = \begin{array}{c} \text{---} \\ | \quad | \\ \text{---} \end{array}. \quad (38)$$

The identity (37) can be graphically represented for $e = 2$ by using the folded picture, where we fold the ket $|\text{GHZ}\rangle$ behind the bra $\langle\text{GHZ}|$ and indicate the trace with circles as

$$\begin{array}{c} \circ \quad \circ \\ | \quad | \\ \text{---} \end{array} = \begin{array}{c} \circ \\ | \\ \text{---} \end{array}. \quad (39)$$

We take an initial state $|\psi_0\rangle$ that is a product state of GHZ states, arranged according to the 2-coloring, such that the states correspond to one color and the first layer of unitary gates corresponds to the second color, shown

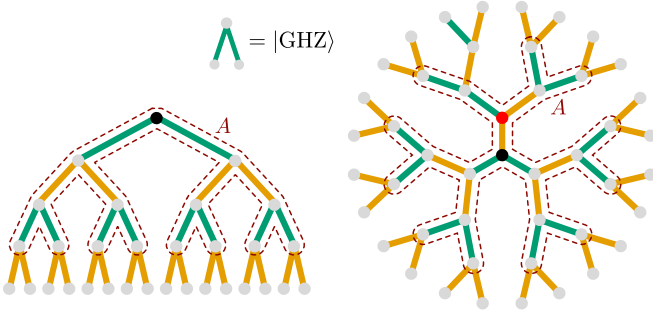


FIG. 7. Regions of the unrooted and rooted trees for which entanglement entropy can be computed exactly using tree-unitarity. Here, GHZ states [Eq. (36)] are placed on green bonds, and the first layer of the circuit is applied to orange bonds. The ‘solvable regions’ for which entanglement can be computed exactly correspond to interiors of light cones. In each case, we show a light cone generated by 3 time steps from the black site. The red site provides a reference for Eq. (56).

in Fig. 7. Using tree-unitarity, the entanglement entropy can be exactly computed for specific solvable subregions A . These subregions correspond to the interior of the light cone starting from any point on the lattice, such as any of the snapshots in Fig. 2(c). For example, the regions shown in Fig. 7 correspond to a light cone after three time steps. We consider the dynamics of the reduced density matrix

$$\rho_A(t) = \text{tr}_A[U(t) |\psi_0\rangle \langle \psi_0| U^\dagger(t)]. \quad (40)$$

Suppose we take a subregion A which consists of a light cone grown from r steps (for example, $r = 3$ in Fig. 7). The calculation of $\rho_A(t)$ for *even* times proceeds as follows:

1. At a fixed time t , we write ρ_A as a tensor network [see below (47)] and use unitarity as far as possible to contract the network outside of region A . This will allow us to fully remove gates and GHZ states only outside of a new boundary, extending the boundary of A by t steps. The new boundary will be called the ‘contraction front’; one can view this as evolving during the process of contracting the network.
2. We then use the GHZ contraction property (39) and tree-unitarity to move the contraction front inwards. This can be performed t times, such that the position of the contraction front at the final time t is t steps *smaller* than region A . Sites which are inside region A , but lie outside the contraction front, are now fully thermalized, and contribute $\ln q$ to the entanglement entropy.
3. When $t = r$, after using unitarity and tree-unitarity, the contraction front has shrunk to its deepest possible position ($r = 0$), and all states within A have been thermalized.

The final contraction front (after using unitarity and tree-unitarity) at *odd* times t will be the same as at $t + 1$ if the initial entanglement of A was 0, and the same as $t - 1$ if the initial entanglement of A was nonzero (i.e. GHZ states cross the boundary of A).

We now illustrate these steps by calculating the entanglement growth on the rooted tree first, because the manipulations involved are simpler to visualize. To do this, we introduce a new notation in terms of what we refer to as a ‘tree-folded’ circuit. This will allow us to represent the state of a rooted tree conveniently in a plane, upon which the computation proceeds as a straightforward generalization of the (1+1)d calculation [14]. The key step in tree-folding is to fold together the $z-1$ legs on the leaves of the z -site gate. For $z = 3$, this is graphically depicted as

$$\begin{array}{c} i' \quad j' \quad k' \\ \text{[Purple Gate]} \\ i \quad j \quad k \end{array} = \begin{array}{c} j' \quad i' \quad k' \\ \text{[Folded Purple Gate]} \\ j \quad i \quad k \end{array} = \begin{array}{c} j' \quad i' k' \\ \text{[Yellow Gate]} \\ j \quad ik \end{array}. \quad (41)$$

In terms of the resulting folded gates, tree-unitarity is then expressed as

$$\begin{array}{c} \text{[Purple Gate]} \\ i \quad j \quad k \quad i' \quad j' \quad k' \end{array} = \begin{array}{c} \text{[Yellow Gate]} \\ j \quad ik \quad j' \quad ik' \end{array} = \begin{array}{c} \text{[Two Legs]} \\ i \quad i' \quad j \quad j' \end{array}. \quad (42)$$

and unitarity as

$$\begin{array}{c} \text{[Yellow Gate]} \\ j \quad ik \quad j' \quad ik' \end{array} = \begin{array}{c} \text{[Two Legs]} \\ i \quad i' \quad j \quad j' \end{array}. \quad (43)$$

Note that the legs on the right-hand side of each folded gate now have a larger Hilbert space compared to the legs on the left-hand side. This is in accord with the general move from unitarity to isometry in this work, which we make explicit in the graphical notation. We also introduce the tree-folded GHZ state

$$\begin{array}{c} i \quad j \quad k \\ \text{[GHZ State]} \end{array} = \begin{array}{c} j \quad i \quad k \\ \text{[Folded GHZ State]} \end{array} = \begin{array}{c} j \quad ik \\ \text{[GHZ State]} \end{array}, \quad (44)$$

where the identity (39) with n folded GHZ states can be represented as

$$\begin{array}{c} \text{[GHZ State]} \\ i \quad j \quad k \quad i' \quad j' \quad k' \end{array} = \begin{array}{c} \text{[GHZ State]} \\ i \quad j \quad k \end{array}. \quad (45)$$

Using this notation, a segment of two layers of the circuit acting on two GHZ states can be written

$$(46)$$

where for clarity we have indicated that time (i.e. layers of the circuit) will run upwards. With this notation established, we now return to our objective of computing (40) for the rooted tree (with $r = 3$, for specificity, corresponding to the region A in Fig. 7). At $t = 2$, the reduced density matrix on the rooted tree can be represented in the folded notation as

$$(47)$$

with the red dashed line separating A from its complement \bar{A} , which is traced over. Following the steps presented above, we use unitarity to remove as many gates as possible outside A

$$(48)$$

We see that unitarity has allowed us to disconnect the tensor diagram beyond the contraction front. We can now apply the GHZ contraction property (45), then (folded) tree-unitarity (42), to move the contraction front

inwards:

$$(49)$$

This final expression shows that $\rho_A(t = 2)$ is a unitary transformation of $|\text{GHZ}\rangle \langle \text{GHZ}| \otimes \frac{1}{q^{z(z-1)^2}} \mathbb{1}^{\otimes z(z-1)^2}$, where the original GHZ states closest to the boundary of A have fully thermalized. Since the unitary transformation will not affect the entanglement spectrum, the entanglement entropy is $S_A(t = 2) = z(z-1)^2 \ln q$. We also see that the entanglement spectrum is flat, such that all entanglement entropies are identical; the entanglement dynamics consists solely of growing the rank of the entanglement spectrum while maintaining a uniform distribution over the nontrivial eigenvalues, similar to the case of dual-unitary circuits.

At $t = 4$, after using unitarity in step 1, the initial position of the contraction front has moved outwards by two steps,

$$(50)$$

In this equality we have used the GHZ contraction and tree-unitarity to move the contraction front inside region A , until we can go no further. Observe that, although after step 1 the contraction front is two steps further outside A than for $t = 2$, the additional two layers of gates for $t = 4$ allows us to use the GHZ/tree-unitarity conditions to move the front two steps further inside A than in the $t = 2$ case. For our choice of region with $r = 4$, we explicitly see from the above graphical equation that at all sites are now thermalized, such that $\rho_A(t = 4)$ is a unitary transformation of $\frac{1}{q^n} I^{\otimes n}$, where $n = [(z-1)^4 - 1] / (z-2)$ is the number of sites in A .

The extension to a larger region A of r generations on the rooted tree directly follows: the initial reduced

density matrix will be

$$\rho_A(0) = \bigotimes_{j=0}^{(r-1)/2} (|\text{GHZ}\rangle \langle \text{GHZ}|)^{\otimes (z-1)^{2j}}, \quad (51)$$

and for every two layers of the circuit applied, successive sets of GHZ states (moving inwards from the boundary of A towards the root) will be transformed as

$$(|\text{GHZ}\rangle \langle \text{GHZ}|)^{\otimes (z-1)^{2j}} \rightarrow \frac{1}{q^{z \cdot z^{2j}}} \mathbb{1}^{\otimes z \cdot (z-1)^{2j}} \quad (52)$$

up to a unitary transformation — the process that we termed ‘thermalization’. This therefore will increase the entanglement entropy by $z \cdot (z-1)^{2j} \ln q$, for every two time steps, until saturation when $t = r$.

Translating this into entanglement entropy, and keeping in mind the fact that the number of GHZ states is bigger for increasing r , we find that for even times $t \leq r$,

$$S_A^e(t) = \frac{(z-1)^{r+1}}{z-2} (1 - (z-1)^{-t}) \ln q, \quad (53)$$

and for odd times $t \leq r$

$$S_A^o(t) = S_A^e(t+1). \quad (54)$$

For $t \geq r$, the entanglement entropy saturates to its maximum value

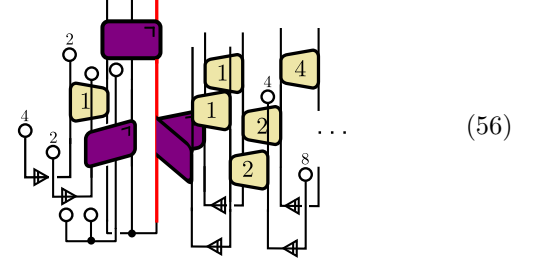
$$S_\infty = \frac{(z-1)^{r+1} - 1}{z-2} \ln q. \quad (55)$$

We emphasize that this result applies independent of the specific choice of tree-unitary gates and furthermore, that there is no requirement that all gates be the same: the only properties used in the calculation are tree-unitarity and the GHZ contraction.

The rooted tree allows for straightforward calculation of the entanglement entropy through the folding trick, but remains slightly unsatisfactory since the root is ascribed a special role. However, the calculation can be adapted to the unrooted tree, for ‘solvable regions’ where A is taken to be the interior of a light cone starting from any point.

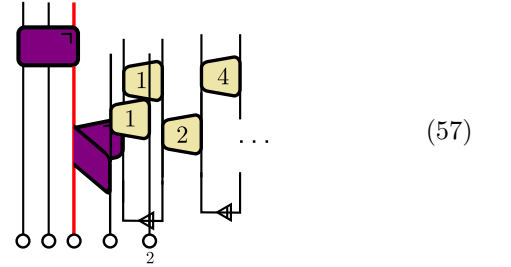
The key idea is that when we choose such a region, the same 3-step process to find $\rho_A(t)$ applies, such that the outermost GHZ states thermalize successively in intervals $\Delta t = 2$, just as for the rooted tree. We will again illustrate this for a region A of radius $r = 3$, as in Fig. 7. First, find the single ‘anomalous’ gate whose root is at the boundary of A (in Fig. 7, this is the green gate connected to the red site). Take the leaf of this gate (i.e. the red site), and fold all other gates from this point just as for the rooted tree. Although not all of these folded legs will have the same ‘radius’, the calculation applies in the same way to all of them — that is, we use unitarity to disconnect the region t steps beyond the boundary, then use tree-unitarity to move this contraction front t steps within the boundary (for even t).

As long as we choose the region A to be enclosed by a lightcone of the unrooted tree, the same principle applies to the anomalous gate too. For even t , unitarity initially places the contraction front t steps from the boundary, with tree-unitarity allowing us to move the contraction front t steps inside. To make this a little more concrete, consider again $\rho_A(t = 2)$. After using unitarity, the part of the tree near the anomalous gate will be



Here, the thickened red line corresponds to the red site in Fig. 7, and the ellipsis indicates that the folded pattern is continued up to the edges of the region. The calculation there will be identical to the rooted tree.

Now we can use GHZ contractions and tree-unitarity to move the contraction front inwards, to 2 steps inside the region A (here, moving inwards by a step means reversing the growth of the light cone by one time step)



The light cone structure allows this process to be continued with further time steps, with the outermost GHZ states thermalizing on alternating time steps as in the case of the rooted tree.

For a light cone of radius r (i.e. generated by r time steps), the number of sites inside this region is

$$n_{LC}(r) = \frac{z}{z-2} [(z-1)^r - 1]. \quad (58)$$

From this, the entanglement entropy after an even time $t \leq r$ will be given by $n_{LC}(r) - n_{LC}(r-t)$, giving

$$S_A^e(t) = z \cdot \frac{(z-1)^r}{z-2} (1 - (z-1)^{-t}) \ln q, \quad (59)$$

whereas for odd time steps, $t \leq r$,

$$S_A^o(t) = S_A^e(t+1). \quad (60)$$

For $t \geq r$, $S(t)$ saturates to its maximum value

$$S_\infty = z \frac{(z-1)^r - 1}{z-2} \ln q. \quad (61)$$

The above results apply when the initial entanglement is 0, with the boundary of A not cutting any GHZ states. If such a boundary is shifted by one, the above formulae are simply shifted by a time step. On the unrooted tree, for *odd* times $t \leq r$,

$$S_A^o(t) = z \cdot \frac{(z-1)^r}{z-2} (1 - (z-1)^{-t}) \ln q \quad (62)$$

and for even times $t \leq r$,

$$S_A^e(t) = S_A^o(t+1), \quad (63)$$

reaching the same S_∞ for $t \geq r$.

Had we not chosen a light cone region, then after using unitarity, there would be insufficiently many contractions to use tree-unitarity in going from (56) to (57). To understand this, note that in the case of a light cone region, the final contraction fronts from different branches will reach the common node of those branches at the same time. This ensures that as we contract inwards, we are always able to trace over $z-1$ pairs of legs. However, with a region that is not a light cone, the final contraction fronts of two branches will reach their common node at different times; in the next time step, we will therefore not be able to contract over enough legs to use tree-unitarity to continue propagating the contraction front inwards. It is worth noting that the idea that the solvable regions for entanglement growth correspond to a light cone region applies also to the rooted tree with the light cone starting from the root, and can be seen as extending the notion of a contiguous region from (1+1)d circuits, in which the light cone region is just a line.

We verify the formulas presented above for the entanglement growth for the rooted and unrooted tree by comparing against classical simulations of Clifford tree-unitary $z=3$ circuits, as shown in Fig. 8. Note that although Clifford circuits can be efficiently simulated in polynomial time in the number of qubits N , the challenge in tree simulations is that N itself grows exponentially with depth r , $N \sim z(z-1)^{r-1}$.

V. MAXIMUM VELOCITY TREE-UNITARY CIRCUITS

In the previous section, we found that tree-unitarity alone does not imply operator spreading with a maximum butterfly velocity, in contrast with the situation for dual-unitary circuits. Fundamentally, this difference is due to the fact that the tree geometry allows the operators to move in multiple directions at a given time step, as opposed to a single direction in (1+1)d. However, by imposing further constraints beyond just tree-unitarity, it is possible to obtain tree-unitary circuits in which operators spread with maximal velocity in either specific directions or *all* directions.

In fact, the latter scenario pertains to the kicked Ising dynamics of Sec. III C. In Fig. 10, we show that for the

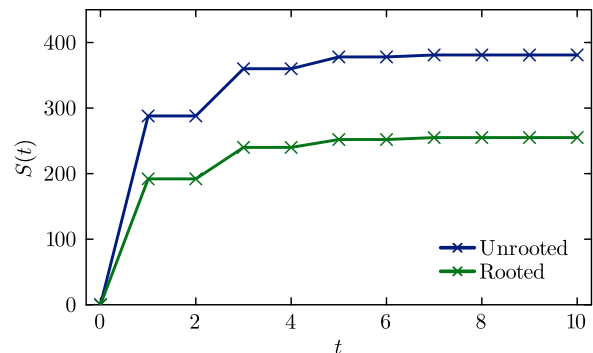


FIG. 8. Entanglement entropy $S(t)$ (in units of $\ln 2$) starting from an exactly solvable GHZ state for a subsystem consisting of the first $r=7$ generations of the unrooted and rooted trees. Crosses are numerical data from simulating a tree-unitary Clifford circuit with $z=3$, and the solid lines correspond to Eqs. (53-55) for the unrooted tree and Eqs. (59-61) for the rooted tree.

KIM the OTOC approaches a non-trivial value on the light cone (dependent on the choice of operators), indicating a maximal butterfly velocity. This maximal butterfly velocity in all directions can be understood by observing that the KIM satisfies a further set of relations, which we term the *maximum-velocity conditions*. In order for a gate to be maximal velocity from ingoing leg i to outgoing leg $j \neq i$, it needs to be unitary when these gates are swapped, i.e. when it is viewed as a transformation from the z legs consisting of the $z-1$ incoming legs different from i and the outgoing leg j , to the remaining set of z legs consisting of i grouped with the $z-1$ outgoing legs distinct from j . In the folded graphical notation, focusing on $z=3$ and $i=2, j=1$ for concreteness, this condition reads

$$\text{[Diagram]} = \text{[Diagram]}, \quad (64)$$

which is equivalent to tracing over the other set of legs

$$\text{[Diagram]} = \text{[Diagram]}. \quad (65)$$

Clearly, there are $z(z-1)$ such maximum-velocity conditions corresponding to the possible choices for the ingoing and outgoing legs. When a gate satisfies the maximum-velocity condition for at least one pair of ingoing and outgoing legs, we shall term it a maximum-velocity gate.

The maximum-velocity conditions are stronger than tree-unitarity, since unitarity is stronger than isometry. Put differently, the maximum-velocity condition (64) automatically implies the corresponding tree-unitarity condition (6). In the same way that dual-unitarity implies

a maximal butterfly velocity, imposing the maximal velocity condition between sites i and j implies maximal operator spreading from site i to site j . Considering Eq. (64) (where $i = 2, j = 1$) for concreteness, this identity implies that $\text{tr}_1[U^\dagger \sigma(2)U] = 0$. As discussed in the context of correlation functions, tree-unitarity implies that $U^\dagger(\mathbb{1} \otimes \sigma \otimes \mathbb{1})U$ can only have single-site Pauli contributions where the single-site Pauli matrix ‘hops’ to another site. This additional condition, however, implies that only terms in which there is a Pauli matrix on site 1 can appear. As such, the operator front necessarily moves to site 1. More generally, if tracing over all ingoing legs except for i and tracing over the single outgoing leg j yields the identity (i.e. the maximum-velocity condition between i and j is satisfied), then the operator front initially localized at site i necessarily grows to site j . This property manifests itself as a non-trivial light cone OTOC in the $i \rightarrow j$ direction.

To see this more formally, consider the channel $\mathcal{T}_{e\tilde{e}}$ introduced in Sec. IV B [Eq. (32)]. If the circuit satisfies the maximum-velocity condition for $e \rightarrow \tilde{e}$, then we can construct an additional (left and right) eigenoperator of $\mathcal{T}_{e\tilde{e}}$ with unit eigenvalue:

$$|R'\rangle = \begin{array}{c} \square \\ | \\ \circ \end{array}, \quad \langle L'| = \begin{array}{c} \square \\ | \\ | \end{array}, \quad (66)$$

such that $\mathcal{T}_{e\tilde{e}}|R'\rangle = |R'\rangle$ and $\langle L'|\mathcal{T}_{e\tilde{e}} = \langle L'|$. To understand this, suppose that Eq. (64) is satisfied, such that the circuit is maximum velocity in the $2 \rightarrow 1$ direction. In the four-folded notation, this becomes

$$\begin{array}{c} \circ \quad \circ \\ | \quad | \\ \square \\ | \quad | \\ \circ \quad \circ \end{array} = \begin{array}{c} \circ \\ | \\ \circ \quad \circ \\ | \quad | \\ \circ \quad \circ \end{array} \quad (67)$$

and therefore

$$\mathcal{T}_{21}|R'\rangle = \begin{array}{c} \circ \quad \circ \\ | \quad | \\ \square \\ | \quad | \\ \square \quad \square \\ | \quad | \\ \circ \quad \circ \end{array} = \begin{array}{c} \circ \quad \circ \\ | \quad | \\ \square \quad \square \\ | \quad | \\ \square \quad \square \\ | \quad | \\ \circ \quad \circ \end{array} = \begin{array}{c} \circ \\ | \\ \square \\ | \\ \square \quad \square \\ | \quad | \\ \circ \quad \circ \end{array} = |R'\rangle. \quad (68)$$

The steady-state value of the OTOC on the light cone is set by these non-trivial eigenvalues. From the right eigenstates $|R\rangle$ and $|R'\rangle$ and the left eigenstates $\langle L|$ and $\langle L'|$ we construct a biorthonormal basis

$$|v\rangle = |R\rangle, \quad \langle v'| = \frac{|R'\rangle - q|R\rangle}{\sqrt{q^2 - 1}}, \quad (69)$$

$$\langle v| = \langle L|, \quad \langle v'| = \frac{q\langle L| - \langle L'|}{\sqrt{q^2 - 1}}. \quad (70)$$

satisfying $\langle v|v\rangle = \langle v'|v'\rangle = 1$ and $\langle v'|v\rangle = \langle v|v'\rangle = 0$. At late times we can replace the repeated action of the channel by a projection on these states, i.e.

$$\lim_{t \rightarrow \infty} \mathcal{T}_{e\tilde{e}}^t = |v\rangle\langle v| + |v'\rangle\langle v'| \quad (71)$$

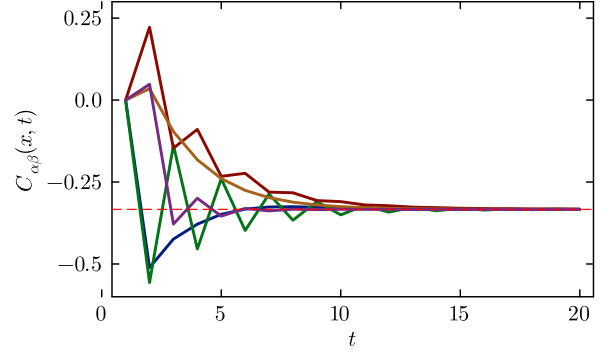


FIG. 9. OTOC $C_{\alpha\beta}(x, t)$ on the light cone direction $2 \rightarrow 3$ with $\sigma_\alpha = \frac{1}{\sqrt{2}}(X + Z)$ and $\sigma_\beta = Z$, for randomly generated maximum-velocity tree-unitary gates (as described in App. B). The OTOC approaches $-1/(q^2 - 1) = -1/3$ on the light cone, as expected from the calculation in the main text.

The OTOC will hence approach a non-trivial value on the light cone

$$\begin{aligned} \lim_{t \rightarrow \infty} C_{\alpha\beta}(i, j; t) &= \langle \sigma_\alpha | v \rangle \langle v | \sigma_\beta \rangle + \langle \sigma_\alpha | v' \rangle \langle v' | \sigma_\beta \rangle \\ &= 1 - \frac{q^2}{q^2 - 1} = \frac{-1}{q^2 - 1}, \end{aligned} \quad (72)$$

where we have evaluated the overlaps as

$$\langle \sigma_\alpha | v \rangle = 1, \quad \langle \sigma_\alpha | v' \rangle = -\frac{q}{\sqrt{q^2 - 1}}, \quad (73)$$

$$\langle v | \sigma_\beta \rangle = 1, \quad \langle v' | \sigma_\beta \rangle = \frac{q}{\sqrt{q^2 - 1}}. \quad (74)$$

This value indicates a maximal butterfly velocity as well as maximal scrambling on the edge of the causal light cone. In Fig. 9, we show this for 5 randomly generated maximum-velocity tree-unitary gates (constructed as described in App. B).

Despite their appearance, these additional maximum-velocity conditions (64) are quite natural, since various explicit constructions of tree-unitary gates satisfy one or more maximum-velocity conditions. The KIM of Sec. III C, for example, is maximum velocity between neighbouring legs. It can be directly checked that, for example,

$$\begin{array}{c} \circ \\ | \\ \square \\ | \\ \square \quad \square \\ | \quad | \\ \circ \quad \circ \end{array} = \begin{array}{c} \circ \quad \square \\ | \quad | \\ \square \quad \square \\ | \quad | \\ \square \quad \square \\ | \quad | \\ \circ \quad \circ \end{array} = \begin{array}{c} \circ \quad \square \\ | \quad | \\ \square \quad \square \\ | \quad | \\ \square \quad \square \\ | \quad | \\ \circ \quad \circ \end{array} \\ = \begin{array}{c} \circ \quad \square \\ | \quad | \\ \square \quad \square \\ | \quad | \\ \square \quad \square \\ | \quad | \\ \circ \quad \circ \end{array} = \begin{array}{c} \circ \quad \square \\ | \quad | \\ \square \quad \square \\ | \quad | \\ \square \quad \square \\ | \quad | \\ \circ \quad \circ \end{array}, \quad (75)$$

which constrains $U^\dagger \sigma_\alpha(2)U$ to only generate terms of the form $\sigma \otimes \sigma \otimes \sigma$ or $\sigma \otimes \mathbb{1} \otimes \sigma$. In fact, for ingoing site 2 the

KIM satisfies an additional identity, as proven in App. C,

$$(76)$$

which additionally removes the possibility of $\sigma \otimes \mathbb{1} \otimes \sigma$ terms.

The prediction $-1/(q^2 - 1)$ assumes that there are no other nontrivial unit-modulus eigenoperators; for the KIM, more eigenoperators can be constructed, giving rise to a light cone OTOC value that depends on the choice of operators Fig. 10 (see App. C). Taking the KIM again, for an operator initially at the root of a gate in the first layer, all correlation functions vanish, indicating maximum ergodicity. The only non-vanishing correlation functions are for an operator passing from a leaf to the root of the gate always. For higher- z KIM, an operator initially at the root of the gate will spread with maximum velocity to all leaf sites (but unlike $z = 3$, need not remain on the root). An operator initially at a leaf will spread with maximum velocity to the root of the gate, without spreading to the other leaves.

A different class of tree-unitary gates that are maximum velocity in *all* directions are perfect tensors. Perfect tensors (for an even number of legs) encode a unitary transformation between any equal-size bipartitions of their legs, i.e. for $z = 3$ these satisfy

$$(77)$$

The maximum-velocity conditions correspond to a subset of these conditions. For $z = 2$, perfect tensors return dual-unitary gates that are additionally maximally ergodic, i.e. all correlation functions vanish identically after a single time step [73]. Remarkably, for tree-unitary gates this is also the case, but with a much less stringent condition: all correlation functions vanish identically after a single time step provided the gate satisfies at least two maximum-velocity conditions. In the language of Ref. 73, these tree-unitary gates result in *Bernoulli dynamics*. Interestingly, while Bernoulli dynamics cannot be realized for $q = 2$ in dual-unitary gates, moving to tree-unitarity with $z > 2$ directly returns a large class of such models.

This result can be understood by noting that the maximum-velocity condition strongly constrains the quantum channel (22) in the calculation of the correlation functions. If Eq. (64) is satisfied, then $M_{23}(\sigma) = 0$, so correlation functions in the $2 \rightarrow 3$ direction vanish. More generally, if the gate satisfies maximum velocity for $i \rightarrow j$, then $M_{i\bar{e}}(\sigma) = 0$ for $\bar{e} \neq j$. A particular direction being maximum velocity means that no other direction can have non-vanishing correlation functions.

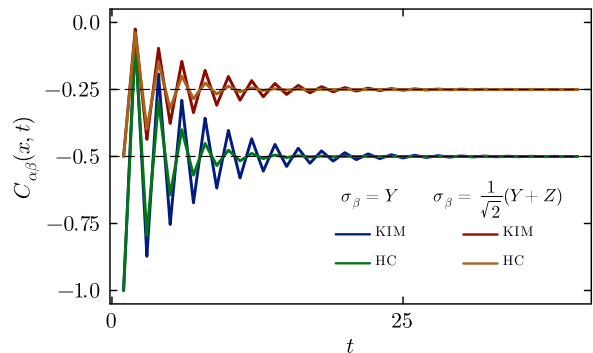


FIG. 10. OTOC $C_{\alpha\beta}(x, t)$ on the light cone direction $2 \rightarrow 3$ with $\sigma_\alpha = \frac{1}{\sqrt{2}}(X + Z)$ and $\sigma_\beta = Y$ or $\sigma_\beta = (Y + Z)/\sqrt{2}$, for the kicked-Ising model (KIM) and a Hadamard-based construction (HC) discussed in App. B. The OTOC approaches the values of -0.5 or -0.25 , in accordance with the calculation in App. C, confirming the operators spread at maximum velocity.

Accordingly, if a gate is maximum velocity in two directions (from a given ingoing leg), then all correlation functions stemming from this ingoing site must vanish. Both perfect tensors and the KIM, along with further constructions which we consider in App. B, are not just maximum velocity but are maximal velocity in more than one direction. All correlation functions therefore vanish, indicating maximum ergodicity on the level of the correlation functions.

VI. CONCLUDING REMARKS

We began this paper with two central objectives. Our first and more conceptual goal was to understand the basic properties of local unitary dynamics on trees. Our second was more technical: namely, to identify a notion of solvability akin to dual-unitarity in one dimension in the resulting “tree+1-dimensional” unitary circuits. The obstacle to the former is the desire to preserve (to the greatest extent possible) the extensively large set of tree symmetries that arise from the freedom to permute the branches at any given node. For the latter, the challenge is that a spatial structure that is a tree clearly cannot admit a space-time duality of the type central to the original formulation of dual-unitarity. (This is in contrast, for example, to problems where the entire dynamical evolution in spacetime is described by a tree tensor network.)

In spite of these challenges, as reported in the preceding sections, we have made substantial progress on both of our main objectives. First, we demonstrated that a seemingly-natural generalization of local unitary dynamics to trees, based on applying 2-site gates according to a z -coloring of the bonds, fails to preserve the tree symmetries — most obviously reflected in the existence of slow and fast portions of the lightcone (despite such patholo-

gies, the resulting circuits allow exact solvability using dual-unitary techniques, summarized for the interested reader in App. D). Instead, we showed that a distinct unitary circuit construction, involving z -site gates applied alternately to sets of sites dictated by a certain bond 2-coloring, results in an isotropic lightcone.

For these z -site-gate circuits we then defined a notion of “tree-unitarity”, that trades the unitary space-time duality for a requirement of space-time isometry between the space-like (tree-like) and time-like directions. Notably, a physically-motivated example of dual-unitarity, the self-dual kicked Ising model, exhibits tree-unitarity when appropriately generalized to the tree setting. Imposing tree-unitarity in turn allowed us to lift much of the solvability of dual-unitary circuits to trees. For example, in tree-unitary circuits, operator correlations vanish except on the lightcone, where they can be exactly computed using quantum channels; the “out-of-time order correlator” (OTOC), a key diagnostic of operator scrambling and quantum chaos, can be computed on the light cone using similar techniques; and exact calculations of entanglement growth are possible for a set of special initial conditions, essentially by ‘folding’ the problem into a one-dimensional system whose Hilbert space dimension grows exponentially with distance from the origin.

However, the move from unitarity to isometry also revealed that tree-unitary quantum circuits are richer than their dual-unitary counterparts. This is especially evident in the computation of OTOC: whereas for dual-unitary circuits the OTOC spreads at the maximum possible “butterfly velocity”, manifesting in nontrivial operator scrambling already *at* the causal lightcone, this is not automatically the case for a generic tree-unitary circuit. Instead, requiring nontrivial OTOCs on the lightcone stems from an additional set of “maximum velocity” conditions, which are not satisfied by generic tree-unitaries. We discuss examples of such maximum-velocity tree-unitary circuits in App. B, but note that the KIM is one such example. This weakening of the connection between solvability and “maximum velocity” means that, in a certain sense, tree-unitary circuits are more ‘generic’ than dual unitaries — at least in their operator scrambling properties.

Having established these new ideas and results, in the remainder of this section we discuss their possible extensions, links to other work, and questions they raise about dynamics more generally.

First, we note that there are other interesting computations one can envisage on the tree, or even locally tree-like graphs. For instance, all our present results make no assumptions of regularity in either space or time (other than, of course, tree-unitarity). However, one can compute additional quantities when such structure is present — as for instance is the case for *Floquet* circuits such as the KIM, that repeat periodically in time. One such quantity is the so-called spectral form factor (SFF) [70], defined as $K(t) = \text{Tr}[U^t]$, where U is the unitary evolution operator for a single full time step (in our case, corre-

sponding to a single application of gates on each of the disjoint sets of bonds). The SFF encodes correlations between the eigenphases of the Floquet operator U , and as such is a sensitive spectral probe of chaos (complementing the OTOC). One challenge in computing the SFF is that it is not self-averaging, necessitating the introduction of some sort of disorder averaging to obtain sensible results. While such an analytic computation may be feasible on a tree, a more subtle issue is to interpret the result, since the thermodynamic limit of locally tree-like problems is often subtle⁴. Numerical computations are challenged both by the exponential growth of the system size with depth, and, more seriously, by the finite bulk-boundary ratio; it is hence crucial to identify ways to consider “closed” trees by suitably rewiring sites on the boundary. Addressing these issues, both for the computation of the SFF and more generally, is an important direction for future work.

This connects naturally to the broader question of extending tree-unitarity to more general “expander” graphs, such as hyperbolic lattices, that share a similar finite bulk-boundary ratio for subsystems. The crucial new feature in such settings, in common with the closed trees mentioned above, is the presence of loops (which are usually short in the former case, and long in the latter). Implementing tree-unitary-type solvability in the presence of loops is a question to which we have no clear answer at the present time — yet one that is clearly important to address, given the relevance of expanders to quantum error correction and related ideas [41–45]. One promising direction towards this objective is to utilize techniques such as the cavity method [74–78] and belief propagation [79–81] that have proven to be powerful tools in more conventional statistical mechanics problems on trees. In a different direction, multi-unitary gates arranged on expander graphs have gained interest as holographic codes, and it is natural to explore how tree-unitarity modifies e.g. the coding properties and correlation structure within such models [54–57].

Even within the tree+1 dimensional unitary setting, there are several open problems that we briefly flag. We have already mentioned the use of Clifford tree unitaries as a means of simulating entanglement growth (albeit for small system sizes due to the exponential-growth problem). Of course, Clifford dynamics is more general and would allow a deeper understanding of non-tree-unitary circuits on trees [82]. A second class of solvable quantum circuits are built from so-called “matchgate” tensors, which can often be mapped to free fermions. Studying such matchgate circuits on trees potentially offers a distinct tractable limit to tree-unitarity [83–86]. A rather different question is whether tree-unitarity can be ex-

⁴ For instance, the spectrum of the adjacency matrix on a tree has distinct thermodynamic limit depending on whether one takes this limit through a sequence of large Cayley trees, or as (a suitable average over) an ensemble of regular random graphs.

tended in a hierarchical manner, as in the case of dual-unitary circuits, where such constructions can lead to circuits with multiple light cones and submaximal entanglement growth [31–35]. Moving away from tree-unitary problems and instead considering Haar-random unitary gates offers an entirely new line of investigation [7, 8]. Such random unitary circuits are usually analytically tractable in the limit of infinite Hilbert space dimension of each individual gate [87–89]. Since for the z -site construction, each gate is a $q^z \times q^z$ unitary, this limit can be accessed by taking *either* q or z to infinity while holding the other fixed. Understanding the differences, if any, between these limits is an intriguing question, as is the development of an ‘entanglement membrane’-like picture for trees [32, 34, 90–92]. For structured models, these different limits should be reflected in the eigenstates of the unitary evolution operator. Eigenstates of systems with local (one-to-one, $z = 2$) and long-range (all-to-all, similar to $z \rightarrow \infty$) interactions have different entanglement structure [93, 94], and it is natural to wonder where tree-like interactions fall in between these limits using e.g. probes of the eigenstate thermalization hypothesis. Still further extensions of both random and tree-unitary circuits are possible by modifying them to include conservation laws [9, 95, 96], and exploring the resulting dynamics.

Breaking unitarity by introducing measurements is yet another possible extension of our work [89, 97–101]. Here, the relevant question is whether there are new insights to be gleaned into the measurement-induced phase transition (MIPT) by moving to the tree setting. Since the boundary of a region now scales in proportion to its volume, we expect scrambling to have a stronger effect than in finite dimension. However, given that MIPTs (characterised by information retained from an initial state) are observed even in all-to-all models [63, 100, 102], an MIPT in tree+1 dimensions seems likely. We note that although dynamical quantum trees have allowed for analytic insight into the MIPT beyond what is achievable in (1+1)d [61, 63], these simplifications are unlikely to hold in the tree+1 setting. Within the tree-unitary setting, one pertinent consideration is if the restricted choice of projective measurements and associated circuit modifications that are necessary in order to preserve solvability [103] are richer than their counterparts in finite dimensional circuits.

Finally, one can consider the z -site tree-unitary gates, but now acting in one dimension. The isometry conditions now offer a different class of dynamics beyond dual-unitarity; it would be interesting to explore the attendant physical consequences.

We could continue to enumerate further new directions, but close here with the hope that answers to those raised above might appear in the not-too-distant future.

ACKNOWLEDGMENTS

We thank Vedika Khemani, Yaodong Li, Frank Pollman, Balázs Pozsgay, Suhail Rather, and Charles Stahl for useful discussions. O.B. and S.A.P. are grateful for the hospitality of the Max Planck Institute for the Physics of Complex Systems in Dresden, where this work was initiated, during an extended visit supported through a 2024 Gutzwiller Award to S.A.P. We also acknowledge support from the UKRI Horizon Europe Guarantee Grant No. EP/Z002419/1 (to S.A.P.). B.P. acknowledges funding through a Leverhulme-Peierls Fellowship at the University of Oxford and the Alexander von Humboldt Foundation through a Feodor-Lynen fellowship. O.B. acknowledges support from a Leverhulme Trust International Professorship [Grant Number LIP-202-014], Merton College, and the Clarendon Fund.

Appendix A: Numerical constructions of general Tree-Unitary Gates

The KIM is an example of a tree-unitary gate which in many ways is non-generic: it is an example of a ‘maximum velocity’ tree-unitary gate, as we discuss in Sec. V. In this section we describe how to construct more generic tree-unitary gates, and thereby numerically estimate the dimensionality of the set of such gates.

To generate ensembles of tree-unitary gates, we extend the method of Ref. 66, which generates dual-unitary gates by iteratively shuffling indices and performing a polar decomposition to find the closest unitary. For clarity, we focus on the $z = 3$ case; the generalization for $z > 3$ is straightforward.

Given a matrix M , with matrix elements $\langle abc|M|def\rangle$, we define ‘reshuffled’ matrices as

$$\langle abde|M_{R_1}|cf\rangle = \langle abc|M|def\rangle, \quad (\text{A1})$$

$$\langle acdf|M_{R_2}|be\rangle = \langle abc|M|def\rangle, \quad (\text{A2})$$

$$\langle bcef|M_{R_3}|ad\rangle = \langle abc|M|def\rangle. \quad (\text{A3})$$

Tree-unitarity of M is the statement that M_{R_i} is an isometry $\forall i$, i.e. $M_{R_i}^\dagger M_{R_i} = \mathbb{1}_{q^2}$.

We now define the map $T_{R_i} : \mathbb{C}^{q^3 \times q^3} \rightarrow \mathbb{C}^{q^3 \times q^3}$ to consist of three stages. First, shuffle the indices to take $M \rightarrow M_{R_i}$. Second, map $M_{R_i} \rightarrow N_{R_i}$ where N_{R_i} is the nearest isometry to M_{R_i} . Finally, unshuffle the indices $N_{R_i} \rightarrow N$. The second step, finding the nearest isometry to M_{R_i} , is achieved by performing a polar decomposition

$$M_{R_i} = N_{R_i} \sqrt{M_{R_i}^\dagger M_{R_i}}, \quad (\text{A4})$$

where N_{R_i} is a $q^4 \times q^2$ matrix satisfying $N_{R_i}^\dagger N_{R_i} = \mathbb{1}_{q^2 \times q^2}$. We shall also need the analogous result for a square matrix: the closest unitary matrix to M is N where $M = N\sqrt{M^\dagger M}$ is the polar decomposition. We shall denote this map $M \rightarrow N$ by T .

Define the composite map $T_c : \mathbb{C}^{q^3 \times q^3} \rightarrow \mathbb{C}^{q^3 \times q^3}$ to act as $T_c(M) = T_{R_3}(T_{R_2}(T_{R_1}(T(M))))$. Given a random $q^3 \times q^3$ ‘seed’ matrix M_0 , we act with T_c a large number of times n to produce a matrix $M_n = T_c^n(M_0)$. If this procedure converges, as numerically seems to be the case for generic initial matrices, it converges to a matrix satisfying all the tree-unitary conditions.

One can generate random tree-unitary gates that satisfy one or more of the maximum-velocity conditions by including this unitarity constraint (in place of the tree-unitarity condition that follows from it) in the above algorithm.

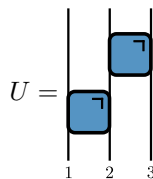
Since we do not have a general parametrization of tree-unitary gates, we numerically estimate the dimensionality of the set of tree-unitary gates. To do this we follow Ref. 27, writing the tree-unitarity constraints as a vector function $\vec{f}(\vec{a}) = 0$ of all real parameters \vec{a} in our matrix. Finding the rank of the Jacobian matrix $\frac{\partial f_i}{\partial a_j}$ gives the (local) dimension of the manifold of solutions to this equation. For 3-site gates with $q = 2$, for each of 100 samples this approach returns that tree-unitary operators form a 37-dimensional space.

Appendix B: Constructions of Tree-Unitary Gates

We now give more explicit examples of tree-unitary gates beyond the KIM. All examples will turn out to be ‘maximum velocity’ as defined in Sec. V in at least one direction. While we do not have any explicit constructions of tree-unitary gates which do not satisfy maximum-velocity conditions, such gates can be obtained numerically using the algorithm described in App. A.

1. Two Dual-Unitary Gates

The first explicit construction consists of two dual-unitary gates applied on adjacent bonds,



$$U = \begin{array}{c} \square \\ \square \end{array} \quad (B1)$$

The entire circuit from this construction could in fact be viewed as a 4-layer circuit of 2-site gates. Tree-unitarity of this composite gate follows directly from dual-unitarity of the 2-site gate.

The maps to calculate light cone correlation functions [Eq. (19) of the main text] here obey $M_{12}(\sigma) = M_{23}(\sigma) = M_{31}(\sigma) = 0$, while $M_{32}(\sigma)$, $M_{13}(\sigma)$, $M_{21}(\sigma) \neq 0$ in general. The indices in Eq. (B1) correspond to our labeling convention of the nodes, with M_{ij} dictating the correlation functions from ingoing leg i to outgoing leg j . Consistent with this, these gates satisfy the maximum-velocity condition for $2 \rightarrow 1$, $1 \rightarrow 3$, and $3 \rightarrow 2$. As

a result, for an operator initially on ingoing leg 2 of a gate in the first layer, correlations are only non-vanishing along the single ray in the $2 \rightarrow 1$ direction, along which operator spreading is maximum velocity. For an operator initially on ingoing leg 1, after one time step the operator will have spread to site 3. This site will then be ingoing leg 2 for the next layer, leading to the single ray $2 \rightarrow 1$. Similarly, an operator initially on ingoing leg 3 will spread to site 1, at which point it will move along the $2 \rightarrow 1$ direction. We see that the maximum-velocity condition here constrains the non-vanishing correlations to be only along that direction. This construction directly extends to higher z , for which $z-1$ dual unitaries applied to different bonds in any order also yields a tree-unitary.

2. Hadamard Construction

A more symmetric example can be constructed from Hadamard matrices and δ -tensors. This 2-site ‘Hadamard construction’ is physically obtained through Ising terms and kicks, like the KIM, but we include Ising couplings between *all* pairs of spins (not just nearest neighbours according to the tree geometry)

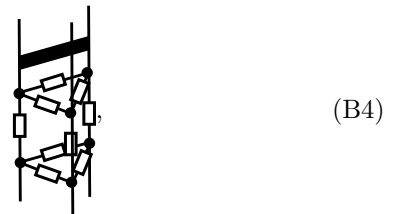
$$U = \prod_{(i,j)}^z \mathcal{I}_{ij} \prod_{j=1}^z \mathcal{K}_j \prod_{(i,j)}^z \mathcal{I}_{ij}, \quad (B2)$$

where \mathcal{I}_{ij} are the Ising terms and \mathcal{K}_j are the kick terms [Eq. (13)], with (i,j) indicating all pairs $i \neq j$. For $z = 3$, this gate is represented as



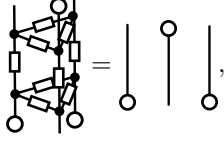
In this construction, the circuit is maximum velocity in all directions, and therefore all two-point correlation functions vanish, $M_{ij}(\sigma) = 0$, as discussed in Sec. V of the main text. The light-cone OTOC is plotted in Fig. 10 of the main text, and tends to the same non-trivial values as the KIM, since it possesses the same additional eigenoperators constructed in App. C.

As with all tree-unitary gates, dressing each outgoing leg with a single-site unitary gate does not alter the tree-unitarity conditions. Furthermore, if we dress this Hadamard construction with a single 2-site unitary,



the maximum-velocity conditions of the original construction imply that we still obey the tree-unitarity conditions. Suppose that the 2-site unitary is applied between

sites 1 and 3. Then the circuit is no longer maximum velocity in the $2 \rightarrow 3$ or $2 \rightarrow 1$ directions, but maintains the maximum velocity along $3 \rightarrow 2$ and $1 \rightarrow 2$. However, the 2-point correlation functions still vanish, because of a further identity satisfied by the gate (see App. C)



$$(B5)$$

which can be interpreted as saying that for the undressed construction,

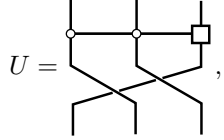
$$U^\dagger(\mathbb{1} \otimes \sigma \otimes \mathbb{1})U \rightarrow \sigma \otimes \sigma \otimes \sigma, \quad (B6)$$

while for the dressed construction

$$U^\dagger(\mathbb{1} \otimes \sigma \otimes \mathbb{1})U \rightarrow \begin{cases} \sigma \otimes \sigma \otimes \sigma \\ \sigma \otimes \sigma \otimes \mathbb{1} \\ \mathbb{1} \otimes \sigma \otimes \sigma \end{cases}. \quad (B7)$$

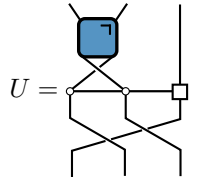
3. Controlled Gates and Tri-Unitary Gates

Tree-unitary gates can also be constructed from a gate with two control qubits and one target qubit, along with SWAP gates



$$(B8)$$

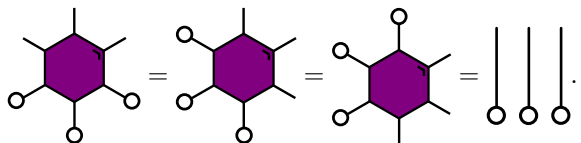
with open circles representing the controls. This gate is maximum velocity in $1 \rightarrow 3$, $2 \rightarrow 1$, and $3 \rightarrow 2$ directions. The extension to higher z is to have $z - 1$ controls, and a cyclic SWAP on all sites. One can further dress this construction with a further SWAP and a dual-unitary gate to obtain



$$(B9)$$

which is also tree-unitary.

Tree-unitary gates acting on three sites can also be obtained from a family of triunitary gates [26], which are 3-site gates satisfying unitarity under $\pi/3$ rotations



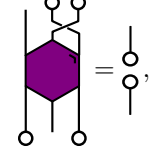
$$(B10)$$

Given a triunitary gate, we can obtain a tree-unitary gate by applying a SWAP to sites 2 and 3 or sites 1 and 2



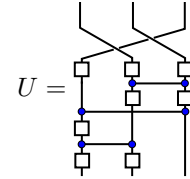
$$(B11)$$

This gate is maximum velocity in the $3 \rightarrow 1$ and $1 \rightarrow 2$ directions. It also satisfies



$$(B12)$$

which is neither a tree-unitary condition nor a maximum-velocity condition, but enforces $M_{21}(\sigma) = M_{22}(\sigma) = 0$. In words, the gate is not maximum velocity from $2 \rightarrow 3$, but for operators starting on site 2 of the gate, they can only have non-zero correlation functions in the $2 \rightarrow 3$ direction. This, along with the maximum-velocity conditions, is what allows for the solvability of the circuits in Ref. 26. Ref. 26 provides a partial parametrization of tri-unitary gates. Using controlled phases $CP_{ij}(\phi) = e^{-i\frac{\phi}{4}(Z_i-1)(Z_j-1)}$ (indicated with blue circles) and single site unitaries (white boxes) we construct the tree-unitary gate



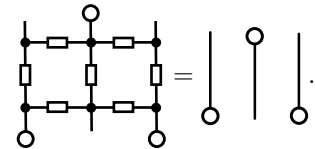
$$(B13)$$

This gives a 31-parameter space of circuits, but is maximum velocity in the $2 \rightarrow 1$, $3 \rightarrow 2$ and $1 \rightarrow 3$ directions, and therefore is highly non-generic. Notice that the dual-unitary construction in Eq. (B1) is contained in this construction as a special case.

Appendix C: Identities for KIM

1. Trace Identity

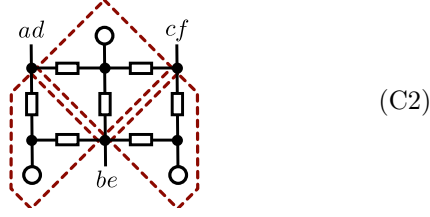
Here we prove an identity for the 3-site KIM used in the main text to constrain the form of Pauli operators under conjugation. We show that



$$(C1)$$

This equality cannot be shown simply using the identities (16), but still relies on the properties of complex

Hadamard matrices. Consider separating out the LHS of (C1) into the following parts



Each of these parts have the form of a δ -tensor surrounded by an equal number of complex Hadamard matrices and their Hermitian conjugates. Our goal will be to show that these parts are themselves (essentially) δ -tensors, following similar arguments as in Ref. 69, from which the identity will follow. The complex Hadamard matrix H [Eq. (12)], making up the kick and the Ising terms, can be written as

$$H = DFD, \quad (\text{C3})$$

where F is the $q = 2$ Fourier matrix

$$F = \begin{pmatrix} 1 & 1 \\ 1 & -1 \end{pmatrix}, \quad (\text{C4})$$

and D is a diagonal matrix with matrix elements $D_{aa} = e^{i\phi_a}$

Since each of the parts above consists of a complex Hadamard and its Hermitian conjugate, the phases on and next to the δ -tensor cancel out. For the parts consisting of two folded gates, this leaves us with

$$\begin{aligned} \text{Diagram} &= \frac{1}{2} e^{i(\phi_a + \phi_e - \phi_a - \phi_b)} \sum_f (-1)^{(f-1)(a+b+d+e-4)} \\ &= e^{i(\phi_a + \phi_e - \phi_a - \phi_b)} \delta_{(a+b+c+d)} \end{aligned} \quad (\text{C5})$$

where $\delta_{(i)} \equiv \delta_{i \bmod 2, 0}$. Similarly, with three folded gates we have

$$\text{Diagram} = e^{i(\phi_a + \phi_e + \phi_f - \phi_a - \phi_b - \phi_c)} \delta_{(a+b+c+d+e+f)}. \quad (\text{C6})$$

Piecing these together in (C2) and cancelling common phase factors, we obtain

$$\delta_{(abde)} \delta_{(abcdef)} \delta_{(bcef)} = \delta_{a,d} \delta_{b,e} \delta_{c,f} \quad (\text{C7})$$

where, e.g. $\delta_{(abde)} \equiv \delta_{(a+b+d+e)}$, and so on. This returns the RHS of the identity (C1) that we set out to show.

2. OTOC Channel Eigenoperators

In Sec. V of the main text, we showed that satisfying a maximum-velocity condition led to a non-trivial eigenoperator with unit-eigenvalue of the OTOC channel. Constructing this eigenoperator explicitly, we showed that

the light cone OTOC approached the value of $-1/(q^2-1)$. The KIM, however, has additional symmetries that allow for the construction of further eigenoperators with eigenvalue 1, changing this non-trivial light cone OTOC value in a way which depends explicitly on the choice of operators, as for the 2-site KIM in Refs. 16 and 104.

Let's briefly recall the status in the main text. The light-cone OTOC is computed using the channel $\mathcal{T}_{e\bar{e}}$ defined by, for example,

$$\mathcal{T}_{23}|\sigma\rangle = \text{Diagram} \quad (\text{C8})$$

Unitarity allows the construction of a single left/right eigenoperator with eigenvalue 1,

$$|R\rangle = \text{Diagram}, \quad |L\rangle = \text{Diagram} \quad (\text{C9})$$

Maximum velocity in the direction $e \rightarrow \bar{e}$ allows the construction of a further left/right eigenoperator with eigenvalue 1,

$$|R'\rangle = \text{Diagram}, \quad |L'\rangle = \text{Diagram} \quad (\text{C10})$$

Without any further structure, these are the only unit-eigenvalue eigenoperators, and from these one can show that the light cone OTOC approaches $-1/(q^2-1)$, as done in the main text. For the KIM, however, we can construct one additional left/right eigenoperator with eigenvalue 1 [104],

$$|R''\rangle = \text{Diagram}, \quad |L''\rangle = \text{Diagram} \quad (\text{C11})$$

We now orthonormalize the first pair as before (with $q = 2$ for the KIM)

$$|v\rangle = |R\rangle, \quad |v'\rangle = \frac{|R'\rangle - 2|R\rangle}{\sqrt{3}}, \quad (\text{C12})$$

$$\langle v| = \langle L|, \quad \langle v'| = \frac{2\langle L| - \langle L'|}{\sqrt{3}}, \quad (\text{C13})$$

with the new eigenoperators orthonormalized to

$$|v''\rangle = \frac{1}{\sqrt{2}} \left(\frac{1}{\sqrt{6}}|R\rangle - \sqrt{\frac{2}{3}}|R'\rangle + \sqrt{\frac{3}{2}}|R''\rangle \right), \quad (\text{C14})$$

$$\langle v''| = \frac{1}{\sqrt{2}} \left(-\sqrt{\frac{2}{3}}\langle L| + \frac{1}{\sqrt{6}}\langle L'| + \sqrt{\frac{3}{2}}\langle L''| \right). \quad (\text{C15})$$

The overlaps required for the OTOC now explicitly depend on the operator. We take $\sigma_\alpha = \alpha_x \sigma_x + \alpha_y \sigma_y +$

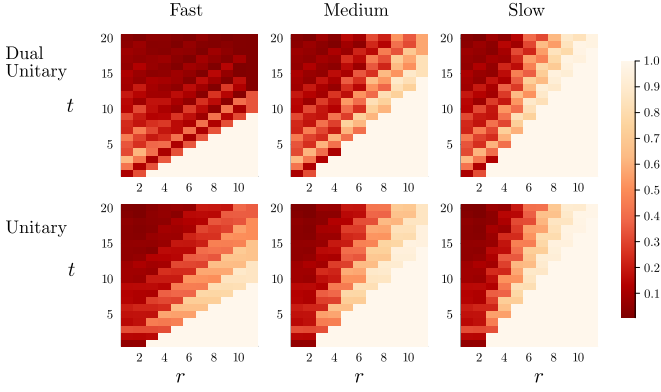


FIG. 11. OTOCs for dual-unitary and unitary circuits on the $z = 3$ tree along fast, medium (alternating fast and slow steps), and slow directions. For dual-unitary circuits in the fastest direction, the OTOC converges to a non-trivial value on the light cone, corresponding to a butterfly velocity $v_B = 1$. In all other directions, and for unitary-only circuits, the typical rate at which operators grow is $v_B < 1$, with a front that broadens in time. The simulations were performed using the QuantumClifford.jl package [105], with the random unitary gates generated using the algorithm in Ref. 106, and random dual-unitary gates from the SDKI-r class introduced in Ref. 101.

2. Out-of-time-order Correlators

In Fig. 11, we plot the OTOC for random Clifford simulations of both dual-unitary and unitary circuits in fast, intermediate, and slow directions. The first aspect to notice is that the asymmetry of the light cone is nicely visible in these plots. Second, on the dual-unitary fast path, the OTOC converges to a non-trivial value, and propagates with a butterfly velocity $v_B = 1$. However, away from the fast direction, we observe a butterfly velocity that is slower than the light velocity, with spreading of the OTOC inside the light-cone. In Fig. 12 we plot the OTOC value on the light cone only in these directions, this time where the dual-unitary gate is the kicked Ising model at the dual-unitary point.

To understand these properties, we follow Ref. 16 and diagrammatically write the OTOC in the form of a quantum channel. We use the same notation developed in the main text in Sec. IV B. As for the correlation functions, we define two maps (using the four-folded notation of the main text)

$$T_1 = \begin{array}{c} \circ \\ | \\ \square \\ | \\ \sigma \\ \square \end{array}, \quad T_2 = \begin{array}{c} \circ \\ | \\ \square \\ | \\ \sigma \\ \square \end{array}, \quad (\text{D5})$$

where each fast step corresponds to T_1 and each slow step for $z = 3$ to $T_1 T_2$.

For unitary gates, right/left eigenoperators of both T_2

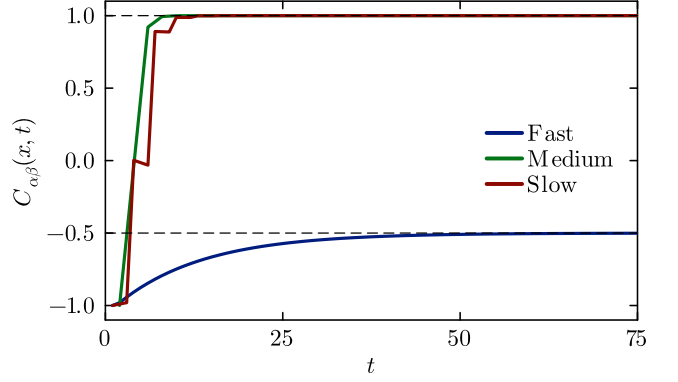


FIG. 12. OTOC for the 2-site brickwork circuit on the tree, where each 2-site gate is the kicked Ising model at its dual-unitary point. Here, $\sigma_\alpha = (X + Z)/\sqrt{2}$ and $\sigma_\beta = Y$. Along the fastest direction the OTOC converges to the non-trivial value of -0.5 . In the slowest direction and a direction consisting of alternating fast/slow steps, the OTOC approaches the trivial value of 1.

and T_1 with eigenvalue 1 are given by

$$|R\rangle = \begin{array}{c} | \\ \square \end{array}, \quad |L\rangle = \begin{array}{c} \circ \\ | \\ \square \end{array}. \quad (\text{D6})$$

Assuming only unitarity, we expect no other unit eigenvalues, and the light cone OTOC approaches the trivial value

$$\begin{aligned} \lim_{t \rightarrow \infty} C_{\alpha\beta}(i, j; t) &= (\sigma_\alpha |R\rangle)(L|\sigma_\beta) \\ &= \begin{array}{c} \sigma_\alpha \circ \\ | \\ \square \\ | \\ \sigma_\beta \square \end{array} = \frac{1}{q^2} \text{tr}[\sigma_\alpha^2] \text{tr}[\sigma_\beta^2] = 1. \end{aligned} \quad (\text{D7})$$

Imposing dual-unitarity on the gates allows one to construct a further left/right eigenoperator pair of T_1 ,

$$|R'\rangle = \begin{array}{c} | \\ \circ \end{array}, \quad |L'\rangle = \begin{array}{c} \square \\ | \\ \square \end{array}. \quad (\text{D8})$$

As a result, the OTOC on the fastest path (which involves only T_1) approaches a non-trivial light cone value [16], indicating butterfly velocity $v_B = 1$. Notably, however, $|R'\rangle$ and $|L'\rangle$ are *not* eigenoperators of T_2 . As a result, paths involving a finite fraction of slow steps have a light cone OTOC which approaches the trivial value of 1, consistent with the observations made in Figs. 11 and 12.

This result is perhaps unsurprising, because the ‘maximum velocity’ condition follows from the ‘always-hop’ property of dual-unitary gates in Eq. (D4). There is no guarantee that operator weight is left behind on the original site, and therefore no guarantee that weight will be moved forwards in a slow step.

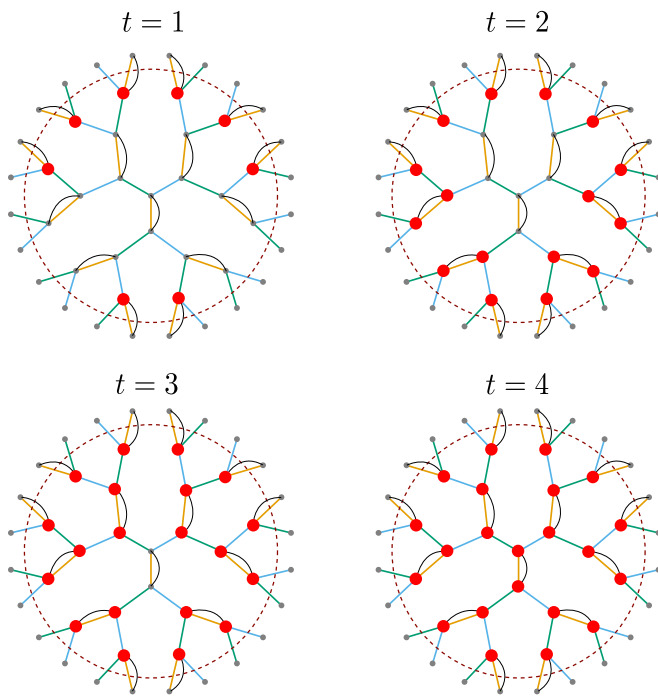


FIG. 13. Here we demonstrate how sites in region A thermalize under dual-unitary dynamics into maximally mixed states. The initial state consists of Bell pairs on orange bonds, shown as the black arcs. We apply the unitary gates in the order orange, green, blue. At each successive time step, Bell pairs across another radial layer thermalize to $\frac{1}{2}\mathbb{1}$ (up to a unitary transformation), shown in red.

3. Entanglement Spreading

As in (1+1)d dual-unitary circuits, the entanglement dynamics can be exactly calculated for specific classes of initial states when the gates are dual-unitary. In particular, we start from a product state, and consider the entanglement entropy (EE) of a region A of r generations from the center (shown in Fig. 13). One solvable class of initial states consists of Bell pairs $\frac{1}{\sqrt{2}}(|\uparrow\uparrow\rangle + |\downarrow\downarrow\rangle)$ on the bonds corresponding to layer z of the circuit. In Fig. 13 with layers applied in the order orange, blue, green, this corresponds to Bell pairs on the green bonds.

To calculate the EE, we construct the reduced density matrix $\rho_A(t) = \text{tr}_{\bar{A}}(U(t)|\psi_0\rangle\langle\psi_0|U^\dagger(t))$. Analogously to the (1+1)d calculation, we use unitarity and dual-unitarity to write $\rho_A(t)$ as a unitary transformation of a

simple state in region A . As an example, we will consider $z = 3$ and a region of size $r = 3$. The number of spins in the layer at radius r is $n(r) = 3 \cdot 2^{r-1}$.

At $t = 0$, all the entanglement comes from the Bell pairs which span the boundary; looking at Fig. 13 we see that there are $\frac{2}{3}n(r) = 2^r$ of these (on the orange bonds). Tracing over \bar{A} , the residual spin of any Bell pair which crosses the boundary is in a maximally mixed state. The reduced density matrix is then $\rho_A(0) = (|\text{Bell}\rangle\langle\text{Bell}|)^{\otimes(2^r-1)} \otimes (\mathbb{1})^{\otimes 2^r}$, so $S(0) = 2^r$. We show

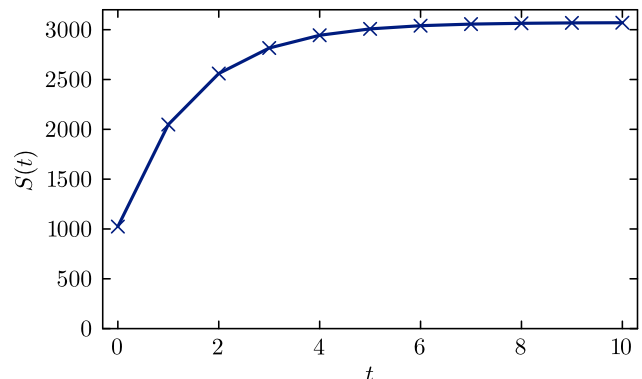


FIG. 14. Entanglement entropy growth for a $z = 3$ tree, under dual-unitary dynamics starting from an exactly solvable Bell pair state for a subsystem A consisting of the first $r = 10$ generations of the tree.

this in Fig. 13 at $t = 0$ by highlighting the sites which contribute a $(\frac{1}{2}\mathbb{1})$ to the reduced density matrix.

For each layer of the circuit applied, the next outermost Bell pairs thermalize. The argument is fully analogous to the (1+1)d case, so we do not repeat it here. This pattern of thermalization leads to an exponentially saturating entanglement entropy, as shown in Fig. 14 for $r = 10$. Since the number of initial Bell pairs between layer r and layer $r + 1$ is 2^r , and noting that Bell pairs on the edge only contribute one site, the entanglement entropy in units of $\ln 2$

$$S(t) = 2^r + (2^{r-1} + \dots + 2^{r-t}) \cdot 2 = 2^r + 2^{r+1}(1 - 2^{-t}). \quad (\text{D9})$$

For general z ,

$$S(t) = (z - 1)^r + \frac{2(z - 1)^r}{z - 2} [1 - (z - 1)^{-t}]. \quad (\text{D10})$$

-
- [1] F. Schäfer, T. Fukuhara, S. Sugawa, Y. Takasu, and Y. Takahashi, Tools for quantum simulation with ultracold atoms in optical lattices, *Nature Reviews Physics* **2**, 411 (2020).
- [2] S. Ebadi, T. T. Wang, H. Levine, A. Keesling, G. Semeghini, A. Omran, D. Bluvstein, R. Samajdar, H. Pichler, W. W. Ho, S. Choi, S. Sachdev, M. Greiner,

- V. Vuletić, and M. D. Lukin, Quantum phases of matter on a 256-atom programmable quantum simulator, *Nat* **595**, 227 (2021).
- [3] R. Blatt and C. F. Roos, Quantum simulations with trapped ions, *Nat. Phys.* **8**, 277 (2012).
- [4] F. Arute, K. Arya, R. Babbush, D. Bacon, J. C. Bardin, R. Barends, R. Biswas, S. Boixo, F. G. S. L.

- Brandao, D. A. Buell, B. Burkett, Y. Chen, Z. Chen, B. Chiaro, R. Collins, W. Courtney, A. Dunsworth, E. Farhi, B. Foxen, A. Fowler, C. Gidney, M. Giustina, R. Graff, K. Guerin, S. Habegger, M. P. Harrigan, M. J. Hartmann, A. Ho, M. Hoffmann, T. Huang, T. S. Humble, S. V. Isakov, E. Jeffrey, Z. Jiang, D. Kafri, K. Kechedzhi, J. Kelly, P. V. Klimov, S. Knysh, A. Korotkov, F. Kostritsa, D. Landhuis, M. Lindmark, E. Lucero, D. Lyakh, S. Mandrà, J. R. McClean, M. McEwen, A. Megrant, X. Mi, K. Michielsen, M. Mohseni, J. Mutus, O. Naaman, M. Neeley, C. Neill, M. Y. Niu, E. Ostby, A. Petukhov, J. C. Platt, C. Quintana, E. G. Rieffel, P. Roushan, N. C. Rubin, D. Sank, K. J. Satzinger, V. Smelyanskiy, K. J. Sung, M. D. Trevithick, A. Vainsencher, B. Villalonga, T. White, Z. J. Yao, P. Yeh, A. Zalcman, H. Neven, and J. M. Martinis, Quantum supremacy using a programmable superconducting processor, *Nat* **574**, 505 (2019).
- [5] Y. Kim, A. Eddins, S. Anand, K. X. Wei, E. Van Den Berg, S. Rosenblatt, H. Nayfeh, Y. Wu, M. Zaletel, K. Temme, and A. Kandala, Evidence for the utility of quantum computing before fault tolerance, *Nat* **618**, 500 (2023).
- [6] M. Nielsen and I. Chuang, *Quantum Computation and Quantum Information* (Cambridge University Press, 2010).
- [7] C. Von Keyserlingk, T. Rakovszky, F. Pollmann, and S. Sondhi, Operator Hydrodynamics, OTOCs, and Entanglement Growth in Systems without Conservation Laws, *Phys. Rev. X* **8**, 021013 (2018).
- [8] A. Nahum, S. Vijay, and J. Haah, Operator Spreading in Random Unitary Circuits, *Phys. Rev. X* **8**, 021014 (2018).
- [9] V. Khemani, A. Vishwanath, and D. A. Huse, Operator Spreading and the Emergence of Dissipative Hydrodynamics under Unitary Evolution with Conservation Laws, *Phys. Rev. X* **8**, 031057 (2018).
- [10] M. P. Fisher, V. Khemani, A. Nahum, and S. Vijay, Random Quantum Circuits, *Annu. Rev. Condens. Ma. P.* **14**, 335 (2023).
- [11] S. Gopalakrishnan and A. Lamacraft, Unitary circuits of finite depth and infinite width from quantum channels, *Phys. Rev. B* **100**, 064309 (2019).
- [12] B. Bertini, P. Kos, and T. Prosen, Exact Correlation Functions for Dual-Unitary Lattice Models in $1 + 1$ Dimensions, *Phys. Rev. Lett.* **123**, 210601 (2019).
- [13] P. W. Claeys and A. Lamacraft, Ergodic and Nonergodic Dual-Unitary Quantum Circuits with Arbitrary Local Hilbert Space Dimension, *Phys. Rev. Lett.* **126**, 100603 (2021).
- [14] B. Bertini, P. Kos, and T. Prosen, Entanglement Spreading in a Minimal Model of Maximal Many-Body Quantum Chaos, *Phys. Rev. X* **9**, 021033 (2019).
- [15] T. Zhou and A. W. Harrow, Maximal entanglement velocity implies dual unitarity, *Phys. Rev. B* **106**, L201104 (2022).
- [16] P. W. Claeys and A. Lamacraft, Maximum velocity quantum circuits, *Phys. Rev. Research* **2**, 033032 (2020).
- [17] B. Bertini and L. Piroli, Scrambling in random unitary circuits: Exact results, *Phys. Rev. B* **102**, 064305 (2020).
- [18] W. W. Ho and S. Choi, Exact Emergent Quantum State Designs from Quantum Chaotic Dynamics, *Phys. Rev. Lett.* **128**, 060601 (2022).
- [19] P. W. Claeys and A. Lamacraft, Emergent quantum state designs and biunitarity in dual-unitary circuit dynamics, *Quantum* **6**, 738 (2022).
- [20] M. Ippoliti and W. W. Ho, Dynamical Purification and the Emergence of Quantum State Designs from the Projected Ensemble, *PRX Quantum* **4**, 030322 (2023).
- [21] D. T. Stephen, W. W. Ho, T.-C. Wei, R. Raussendorf, and R. Verresen, Universal Measurement-Based Quantum Computation in a One-Dimensional Architecture Enabled by Dual-Unitary Circuits, *Phys. Rev. Lett.* **132**, 250601 (2024).
- [22] P. W. Claeys and G. De Tomasi, Fock-Space Delocalization and the Emergence of the Porter-Thomas Distribution from Dual-Unitary Dynamics, *Phys. Rev. Lett.* **134**, 050405 (2025).
- [23] E. Chertkov, J. Bohnet, D. Francois, J. Gaebler, D. Gresh, A. Hankin, K. Lee, D. Hayes, B. Neyenhuis, R. Stutz, A. C. Potter, and M. Foss-Feig, Holographic dynamics simulations with a trapped-ion quantum computer, *Nat. Phys.* **18**, 1074 (2022).
- [24] X. Mi, P. Roushan, C. Quintana, S. Mandrà, J. Marshall, C. Neill, F. Arute, K. Arya, J. Atalaya, R. Babush, J. C. Bardin, R. Barends, J. Basso, A. Bengtsson, S. Boixo, A. Bourassa, M. Broughton, B. B. Buckley, D. A. Buell, B. Burkett, N. Bushnell, Z. Chen, B. Chiaro, R. Collins, W. Courtney, S. Demura, A. R. Derk, A. Dunsworth, D. Eppens, C. Erickson, E. Farhi, A. G. Fowler, B. Foxen, C. Gidney, M. Giustina, J. A. Gross, M. P. Harrigan, S. D. Harrington, J. Hilton, A. Ho, S. Hong, T. Huang, W. J. Huggins, L. B. Ioffe, S. V. Isakov, E. Jeffrey, Z. Jiang, C. Jones, D. Kafri, J. Kelly, S. Kim, A. Kitaev, P. V. Klimov, A. N. Korotkov, F. Kostritsa, D. Landhuis, P. Laptev, E. Lucero, O. Martin, J. R. McClean, T. McCourt, M. McEwen, A. Megrant, K. C. Miao, M. Mohseni, S. Montazeri, W. Mruzckiewicz, J. Mutus, O. Naaman, M. Neeley, M. Newman, M. Y. Niu, T. E. O'Brien, A. Opremcak, E. Ostby, B. Pato, A. Petukhov, N. Redd, N. C. Rubin, D. Sank, K. J. Satzinger, V. Shvarts, D. Strain, M. Szalay, M. D. Trevithick, B. Villalonga, T. White, Z. J. Yao, P. Yeh, A. Zalcman, H. Neven, I. Aleiner, K. Kechedzhi, V. Smelyanskiy, and Y. Chen, Information scrambling in quantum circuits, *Sci* **374**, 1479 (2021).
- [25] L. E. Fischer, M. Leahy, A. Eddins, N. Keenan, D. Ferracin, M. A. C. Rossi, Y. Kim, A. He, F. Pietracaprina, B. Sokolov, S. Dooley, Z. Zimborás, F. Tacchino, S. Maniscalco, J. Gool, G. García-Pérez, I. Tavernelli, A. Kandala, and S. N. Filippov, Dynamical simulations of many-body quantum chaos on a quantum computer (2024), [arXiv:2411.00765](https://arxiv.org/abs/2411.00765).
- [26] C. Jonay, V. Khemani, and M. Ippoliti, Triunitary quantum circuits, *Phys. Rev. Research* **3**, 043046 (2021).
- [27] T. Prosen, Many-body quantum chaos and dual-unitarity round-a-face, *Chaos: An Interdisciplinary Journal of Nonlinear Science* **31**, 093101 (2021).
- [28] P. W. Claeys, A. Lamacraft, and J. Vicary, From dual-unitary to biunitary: a 2-categorical model for exactly-solvable many-body quantum dynamics, *J. Phys. Math. Theor.* **57**, 335301 (2024).
- [29] R. Suzuki, K. Mitarai, and K. Fujii, Computational power of one- and two-dimensional dual-unitary quantum circuits, *Quantum* **6**, 631 (2022), 2103.09211.
- [30] R. M. Milbradt, L. Scheller, C. Afamus, and C. B. Mendl, Ternary Unitary Quantum Lattice Models and Circuits

- in $2 + 1$ Dimensions, *Phys. Rev. Lett.* **130**, 090601 (2023).
- [31] X.-H. Yu, Z. Wang, and P. Kos, Hierarchical generalization of dual unitarity, *Quantum* **8**, 1260 (2024), 2307.03138.
- [32] M. A. Rampp, S. A. Rather, and P. W. Claeys, Entanglement membrane in exactly solvable lattice models, *Phys. Rev. Res.* **6**, 033271 (2024).
- [33] M. A. Rampp, S. A. Rather, and P. W. Claeys, Geometric constructions of generalized dual-unitary circuits from biunitarity (2024), [arxiv.org:2411.07783](https://arxiv.org/abs/2411.07783).
- [34] A. Foligno, P. Kos, and B. Bertini, Quantum Information Spreading in Generalized Dual-Unitary Circuits, *Phys. Rev. Lett.* **132**, 250402 (2024).
- [35] C. Liu and W. W. Ho, Solvable entanglement dynamics in quantum circuits with generalized space-time duality, *Phys. Rev. Res.* **7**, L012011 (2025).
- [36] A. J. Kollár, M. Fitzpatrick, and A. A. Houck, Hyperbolic lattices in circuit quantum electrodynamics, *Nat* **571**, 45 (2019).
- [37] A. Periwal, E. S. Cooper, P. Kunkel, J. F. Wienand, E. J. Davis, and M. Schleier-Smith, Programmable interactions and emergent geometry in an array of atom clouds, *Nat* **600**, 630 (2021).
- [38] J. Ramette, J. Sinclair, Z. Vendeiro, A. Rudelis, M. Cetina, and V. Vuletić, Any-to-any connected cavity-mediated architecture for quantum computing with trapped ions or Rydberg arrays, *PRX Quantum* **3**, 010344 (2022).
- [39] Q. Xu, J. P. Bonilla Ataides, C. A. Pattison, N. Raveendran, D. Bluvstein, J. Wurtz, B. Vasić, M. D. Lukin, L. Jiang, and H. Zhou, Constant-overhead fault-tolerant quantum computation with reconfigurable atom arrays, *Nat. Phys.* **20**, 1084 (2024).
- [40] D. Bluvstein, S. J. Evered, A. A. Geim, S. H. Li, H. Zhou, T. Manovitz, S. Ebadi, M. Cain, M. Kalinowski, D. Hangleiter, J. P. Bonilla Ataides, N. Maskara, I. Cong, X. Gao, P. Sales Rodriguez, T. Karolyshyn, G. Semeghini, M. J. Gullans, M. Greiner, V. Vuletić, and M. D. Lukin, Logical quantum processor based on reconfigurable atom arrays, *Nat* **626**, 58 (2024).
- [41] N. P. Breuckmann and B. M. Terhal, Constructions and noise threshold of hyperbolic surface codes, *IEEE Trans. Inf. Theory* **62**, 3731 (2016).
- [42] N. P. Breuckmann, C. Vuillot, E. Campbell, A. Krishna, and B. M. Terhal, Hyperbolic and semi-hyperbolic surface codes for quantum storage, *Quantum Sci. Technol.* **2**, 035007 (2017).
- [43] A. Fahimniya, H. Dehghani, K. Bharti, S. Mathew, A. J. Kollár, A. V. Gorshkov, and M. J. Gullans, Fault-tolerant hyperbolic Floquet quantum error correcting codes, [arXiv:2309.10033](https://arxiv.org/abs/2309.10033) (2023).
- [44] O. Higgott and N. P. Breuckmann, Constructions and Performance of Hyperbolic and Semi-Hyperbolic Floquet Codes, *PRX Quantum* **5**, 040327 (2024).
- [45] N. P. Breuckmann and J. N. Eberhardt, Quantum Low-Density Parity-Check Codes, *PRX Quantum* **2**, 040101 (2021).
- [46] T. Rakovszky and V. Khemani, The Physics of (good) LDPC Codes I. Gauging and dualities (2023), [arXiv:2310.16032](https://arxiv.org/abs/2310.16032).
- [47] T. Rakovszky and V. Khemani, The Physics of (good) LDPC Codes II. Product constructions (2024), [arXiv:2402.16831](https://arxiv.org/abs/2402.16831).
- [48] C. L. Baldwin, C. R. Laumann, A. Pal, and A. Scardichio, Clustering of nonergodic eigenstates in quantum spin glasses, *Phys. Rev. Lett.* **118**, 127201 (2017).
- [49] C. Yin, R. Nandkishore, and A. Lucas, Eigenstate localization in a many-body quantum system, *Phys. Rev. Lett.* **133**, 137101 (2024).
- [50] W. De Roeck, V. Khemani, Y. Li, N. O’Dea, and T. Rakovszky, LDPC stabilizer codes as gapped quantum phases: stability under graph-local perturbations (2024), [arXiv:2411.02384](https://arxiv.org/abs/2411.02384).
- [51] C. Yin and A. Lucas, Low-density parity-check codes as stable phases of quantum matter (2024), [arXiv:2411.01002](https://arxiv.org/abs/2411.01002).
- [52] Y. Hong, J. Guo, and A. Lucas, Quantum memory at nonzero temperature in a thermodynamically trivial system, *Nat. Commun.* **16**, 316 (2025).
- [53] B. Placke, T. Rakovszky, N. P. Breuckmann, and V. Khemani, Topological Quantum Spin Glass Order and its realization in qLDPC codes (2024), [arXiv:2412.13248](https://arxiv.org/abs/2412.13248).
- [54] F. Pastawski, B. Yoshida, D. Harlow, and J. Preskill, Holographic quantum error-correcting codes: toy models for the bulk/boundary correspondence, *J. High Energ. Phys.* **2015** (6), 149.
- [55] G. Evenbly, Hyper-invariant tensor networks and holography, *Phys. Rev. Lett.* **119**, 141602 (2017).
- [56] D. Harlow, TASI Lectures on the Emergence of the Bulk in AdS/CFT, [arXiv:1802.01040v](https://arxiv.org/abs/1802.01040v) (2018).
- [57] R. Bistron, M. Hontarenko, and K. Życzkowski, Bulk-boundary correspondence from hyperinvariant tensor networks, *Phys. Rev. D* **111**, 026006 (2025).
- [58] P. D. Gujrati, Bethe or Bethe-like lattice calculations are more reliable than conventional mean-field calculations, *Phys. Rev. Lett.* **74**, 809 (1995).
- [59] G. M. Sommers, D. A. Huse, and M. J. Gullans, Dynamically generated concatenated codes and their phase diagrams (2024), 2409.13801.
- [60] C. R. Laumann, S. A. Parameswaran, and S. L. Sondhi, Absence of Goldstone bosons on the Bethe lattice, *Phys. Rev. B* **80**, 10.1103/physrevb.80.144415 (2009).
- [61] X. Feng, B. Skinner, and A. Nahum, Measurement-Induced Phase Transitions on Dynamical Quantum Trees, *PRX Quantum* **4**, 030333 (2023).
- [62] V. Ravindranath, Y. Han, and X. Chen, Entanglement transitions in noisy quantum circuits on trees (2025), [arXiv:2503.05027](https://arxiv.org/abs/2503.05027).
- [63] A. Nahum, S. Roy, B. Skinner, and J. Ruhman, Measurement and Entanglement Phase Transitions in All-To-All Quantum Circuits, on Quantum Trees, and in Landau-Ginsburg Theory, *PRX Quantum* **2**, 010352 (2021).
- [64] X. Feng, N. Fishchenko, S. Gopalakrishnan, and M. Ippoliti, Charge and Spin Sharpening Transitions on Dynamical Quantum Trees (2024), [arXiv:2405.13894](https://arxiv.org/abs/2405.13894).
- [65] D. Nagaj, E. Farhi, J. Goldstone, P. Shor, and I. Sylvester, Quantum transverse-field Ising model on an infinite tree from matrix product states, *Phys. Rev. B* **77**, 214431 (2008).
- [66] S. A. Rather, S. Aravinda, and A. Lakshminarayanan, Creating Ensembles of Dual Unitary and Maximally Entangling Quantum Evolutions, *Phys. Rev. Lett.* **125**, 070501 (2020).

- [67] M. Akila, D. Waltner, B. Gutkin, and T. Guhr, Particle-time duality in the kicked Ising spin chain, *J. Phys. Math. Theor.* **49**, 375101 (2016).
- [68] B. Gutkin, P. Braun, M. Akila, D. Waltner, and T. Guhr, Exact local correlations in kicked chains, *Phys. Rev. B* **102**, 174307 (2020).
- [69] P. W. Claeys and A. Lamacraft, Operator dynamics and entanglement in space-time dual Hadamard lattices, *J. Phys. A: Math. Theor.* **57**, 405301 (2024).
- [70] B. Bertini, P. Kos, and T. Prosen, Exact Spectral Form Factor in a Minimal Model of Many-Body Quantum Chaos, *Phys. Rev. Lett.* **121**, 264101 (2018).
- [71] M. A. Rampp, R. Moessner, and P. W. Claeys, From Dual Unitarity to Generic Quantum Operator Spreading, *Phys. Rev. Lett.* **130**, 130402 (2023).
- [72] L. Piroli, B. Bertini, J. I. Cirac, and T. Prosen, Exact dynamics in dual-unitary quantum circuits, *Phys. Rev. B* **101**, 094304 (2020).
- [73] S. Aravinda, S. A. Rather, and A. Lakshminarayan, From dual-unitary to quantum Bernoulli circuits: Role of the entangling power in constructing a quantum ergodic hierarchy, *Phys. Rev. Research* **3**, 043034 (2021).
- [74] M. Mézard, G. Parisi, and M. Virasoro, *Spin Glass Theory and Beyond: An Introduction to the Replica Method and Its Applications* (World Scientific, 1986).
- [75] M. Mézard and G. Parisi, The Bethe lattice spin glass revisited, *The European Physical Journal B* **20**, 217–233 (2001).
- [76] M. Mézard and G. Parisi, The cavity method at zero temperature, *J. Stat. Phys.* **111**, 1–34 (2003).
- [77] C. Laumann, A. Scardicchio, and S. L. Sondhi, Cavity method for quantum spin glasses on the Bethe lattice, *Phys. Rev. B* **78**, 134424 (2008).
- [78] C. R. Laumann, S. A. Parameswaran, S. L. Sondhi, and F. Zamponi, AKLT models with quantum spin glass ground states, *Phys. Rev. B* **81**, 174204 (2010).
- [79] R. Alkabetz and I. Arad, Tensor networks contraction and the belief propagation algorithm, *Phys. Rev. Research* **3**, 023073 (2021).
- [80] J. Tindall, M. Fishman, E. M. Stoudenmire, and D. Sels, Efficient tensor network simulation of IBM’s eagle kicked Ising experiment, *PRX Quantum* **5**, 010308 (2024).
- [81] M. Mézard and A. Montanari, *Information, Physics, and Computation* (Oxford University Press, 2009).
- [82] S. Aaronson and D. Gottesman, Improved simulation of stabilizer circuits, *Phys. Rev. A* **70**, 052328 (2004).
- [83] R. Jozsa and A. Miyake, Matchgates and classical simulation of quantum circuits, *Proceedings of the Royal Society A: Mathematical, Physical and Engineering Sciences* **464**, 3089–3106 (2008).
- [84] L. G. Valiant, Quantum circuits that can be simulated classically in polynomial time, *SIAM J. Comput.* **31**, 1229–1254 (2002).
- [85] A. M. Projansky, J. T. Heath, and J. D. Whitfield, Entanglement spectrum of matchgate circuits with universal and non-universal resources, *Quantum* **8**, 1432 (2024).
- [86] P. Richelli, K. Schoutens, and A. Zorzato, Brick wall quantum circuits with global fermionic symmetry, *SciPost Phys.* **17**, 087 (2024).
- [87] A. Chan, A. De Luca, and J. Chalker, Solution of a Minimal Model for Many-Body Quantum Chaos, *Phys. Rev. X* **8**, 041019 (2018).
- [88] A. Chan, A. De Luca, and J. Chalker, Spectral statistics in spatially extended chaotic quantum many-body systems, *Phys. Rev. Lett.* **121**, 060601 (2018).
- [89] C.-M. Jian, Y.-Z. You, R. Vasseur, and A. W. W. Ludwig, Measurement-induced criticality in random quantum circuits, *Phys. Rev. B* **101**, 104302 (2020).
- [90] A. Nahum, J. Ruhman, S. Vijay, and J. Haah, Quantum entanglement growth under random unitary dynamics, *Phys. Rev. X* **7**, 031016 (2017).
- [91] T. Zhou and A. Nahum, Entanglement membrane in chaotic many-body systems, *Phys. Rev. X* **10**, 031016 (2020).
- [92] G. M. Sommers, S. Gopalakrishnan, M. J. Gullans, and D. A. Huse, Zero-temperature entanglement membranes in quantum circuits, *Phys. Rev. B* **110**, 064311 (2024).
- [93] L. D’Alessio, Y. Kafri, A. Polkovnikov, and M. Rigol, From quantum chaos and eigenstate thermalization to statistical mechanics and thermodynamics, *Adv. Phys.* **65**, 239 (2016).
- [94] N. Defenu, A. Lerose, and S. Pappalardi, Out-of-equilibrium dynamics of quantum many-body systems with long-range interactions, *Phys. Rep.* **1074**, 1 (2024).
- [95] J. Richter, O. Lunt, and A. Pal, Transport and entanglement growth in long-range random Clifford circuits, *Phys. Rev. Research* **5**, L012031 (2023).
- [96] A. Foligno, P. Calabrese, and B. Bertini, Nonequilibrium dynamics of charged dual-unitary circuits, *PRX Quantum* **6**, 010324 (2025).
- [97] B. Skinner, J. Ruhman, and A. Nahum, Measurement-Induced Phase Transitions in the Dynamics of Entanglement, *Phys. Rev. X* **9**, 031009 (2019).
- [98] A. Chan, R. M. Nandkishore, M. Pretko, and G. Smith, Unitary-projective entanglement dynamics, *Phys. Rev. B* **99**, 224307 (2019).
- [99] S. Choi, Y. Bao, X.-L. Qi, and E. Altman, Quantum error correction in scrambling dynamics and measurement-induced phase transition, *Phys. Rev. Lett.* **125**, 030505 (2020).
- [100] M. J. Gullans and D. A. Huse, Dynamical Purification Phase Transition Induced by Quantum Measurements, *Phys. Rev. X* **10**, 041020 (2020).
- [101] J. Yao and P. W. Claeys, Temporal entanglement barriers in dual-unitary Clifford circuits with measurements, *Phys. Rev. Research* **6**, 043077 (2024).
- [102] S. Vijay, Measurement-driven phase transition within a volume-law entangled phase (2020), [arXiv:2005.03052](https://arxiv.org/abs/2005.03052).
- [103] P. W. Claeys, M. Henry, J. Vicary, and A. Lamacraft, Exact dynamics in dual-unitary quantum circuits with projective measurements, *Phys. Rev. Research* **4**, 043212 (2022).
- [104] B. Bertini, P. Kos, and T. Prosen, Operator Entanglement in Local Quantum Circuits I: Chaotic Dual-Unitary Circuits, *SciPost Phys.* **8**, 067 (2020).
- [105] S. Krastanov, F. Ahmad, P. Viswanathan, S. Pardi, J. Lapeyre, A. Micciche, Rabqubit, T. Hofmann, gsommers, L. Göttgens, Q. Preiß, IsaacP1234, A. Bhatt, A. Meligrana, Benzillaist, C. Zhao, ShuGeMIT, T. Holy, T. Dang, adrianariton, and ismoldayev, [QuantumSavory/quantumclifford.jl: v0.9.16](https://github.com/QuantumSavory/quantumclifford.jl) (2024).
- [106] S. Bravyi and D. Maslov, Hadamard-free circuits expose the structure of the Clifford group, *IEEE Trans. Inf. Theory* **67**, 4546–4563 (2021).